Bending and free vibration analysis of functionally graded graphene vs. carbon nanotube reinforced composite plates

Enrique García-Macías[a,*], Luis Rodríguez-Tembleque[a], Andrés Sáez[a]

[a]*Department of Continuum Mechanics and Structural Analysis, School of Engineering, Universidad de Sevilla, Spain*

Abstract

Carbon-based nanomaterials have drawn the attention of a large section of the scientific community in recent years. Most research has focused on carbon nanotubes after some experimental studies reported outstanding enhancements of the mechanical properties of polymeric matrices doped with small filler concentrations. Nevertheless, some limiting factors such as high manufacturing cost and difficulty in obtaining adequate uniform dispersions still remain an obstacle to the extensive manufacturing of these composites. Conversely, recent investigations demonstrate the superior properties of graphene, as well as better dispersion and relatively low manufacturing cost. Although these recent findings have begun to turn the attention towards graphene, the number of publications dealing with the theoretical analysis of graphene-reinforced structural elements is rather scant. In this context, the present work reports the bending and vibrational behavior of functionally graded graphene- and carbon nanotube-reinforced composite flat plates. The macroscopic elastic moduli of the composites are computed by means of the Mori-Tanaka model. The results demonstrate superior load bearing capacity of graphene-reinforced composite plates for both fully aligned and randomly oriented filler configurations. In addition, defects in the microstructure stemming from agglomeration and restacking of graphene sheets into graphite platelets are also analyzed.

Keywords:
Agglomeration, Carbon nanotubes, Functionally graded, Graphene, Micromechanics, Restacking

1. Introduction

Over the last two decades, a broad cross section of the scientific community has endeavored to develop carbon-based nanomaterials for high-strength and multifuntional composite materials. In particular, Carbon NanoTubes (CNTs) and graphene have shown promise for developing novel multifunctional nanocomposites [1–6]. CNTs, which can be considered as a rolled-up graphene sheet, have been reported to provide remarkable enhancements of the mechanical properties of polymeric matrices when dispersed at low concentrations [7, 8]. For instance, Qian *et al.* [9] doped polystyrene with a concentration of 1 wt% of Multi-Walled Carbon NanoTubes (MWCNTs), reaching improvements with respect to the neat polymer in the elastic modulus and in the break stress of 36-42% and ~25%, respectively. Notwithstanding the potential of CNTs, aspects such as their high manufacturing cost, difficulty in obtaining adequate uniform dispersions, as well as their highly anisotropic properties, remain an obstacle to the extensive development of CNT-reinforced polymer composites. In contrast, recent investigations agree to indicate the superior properties of graphene and its derivatives [10–13]. It is noteworthy the experimental study of Rafiee *et al.* [14] who compared the effective mechanical properties of epoxy loaded with graphene, Single-Walled Carbon Nanotubes (SWCNTs), and MWCNTs at nanofiller concentrations of 0.1% wt. Their results showed that graphene led to Young's moduli 31% higher than those of pristine epoxy, whilst only 3% increments were reached by SWCNTs. Their results also reported that Graphene sheet-Reinforced Composites (GRCs) outperformed those doped with CNTs in terms of toughness and fatigue behavior. The superiority of graphene is ascribed to its high specific surface area and nanofiller/matrix interlocking, as well as its two-dimensional geometry, which enables more uniform filler distributions in comparison to CNTs. These excellent properties showcased by graphene, together with its low manufacturing cost [15], make GRCs a promising multifunctional composite in the shorter run.

Much research effort has been recently devoted to the synthesis and experimental characterization of GRCs. Stankovich *et al.* [16] first successfully dispersed graphene sheets throughout polystyrene by means of chemical

*Corresponding author.
Email address: egarcia28@us.es (Enrique García-Macías)

reduction of exfoliated Graphite NanoPlatelets (GNPs). Kalaitzidou *et al.* [17] analyzed the morphology and mechanical properties of GNP/polypropylene and showed that, in comparison to available commercial fillers such as carbon fibers, carbon black and clays, GNPs had the strongest reinforcing effect for very low loadings up to 5% in terms of Young's modulus, as well as flexural and impact strength. Ramanathan *et al.* [18] reported the manufacturing of poly(methyl methacrylate) (PMMA) loaded with Functionalized Graphene Sheets (FGSs). Their results showed an outstanding increase of the elastic modulus of 33% with an addition of only 0.05 wt% of FGSs, exceeding those obtained for SWCNT-PMMA composites. Another noteworthy contribution was done by Das *et al.* [19] who studied the nano-indentation response of PolyVinyl Alcohol (PVA) and PMMA doped with FGSs. Their results reported significant increases in both the elastic modulus and hardness with the addition of 0.6 wt% of graphene. Despite these encouraging results from experimentation, the number of research works dealing with the theoretical analysis of GRCs is still rather scarce and, as a consequence, the analysis of the mechanical response of structural elements made of GRCs is at a very early stage. It is worth noting the work by Ji *et al.* [20] who investigated the stiffening effect of graphene sheets dispersed in polymeric materials using the Mori-Tanaka micromechanics method. Their results highlighted the superior stiffening capability of GNPs compared to CNTs. Spanos *et al.* [21] used a micromechanical finite element approach to obtain the mechanical properties of composites reinforced by uniformly distributed GNPs. Rahman and Haque [22] employed Molecular Mechanics (MM) and Molecular Dynamics (MD) simulations to study GNP/epoxy nanocomposites. Among diverse existing approaches, an increasing number of works in the open literature can be found on the application of the modified Halpin-Tsai model for the modeling of GRCs. In this line, a noticeable contribution was done by Feng *et al.* [23] who studied the nonlinear bending behavior of multi-layer polymer nanocomposite beams reinforced with Functionally Graded (FG) distributions of GNPs. In that work, the dosage of GNPs was defined with continuous and smooth functions across the thickness of the beams. An important conclusion of that work was that, in accordance with previous works on other nanoinclusions [24, 25], higher concentrations of GNPs near the top and bottom surfaces of the beams lead to stiffer responses. Similar recent works can be found on the nonlinear bending and thermal postbuckling behaviors of nanocomposite beams in thermal environments and elastic foundations [26], bending and vibrational behavior of FG-GNP-reinforced trapezoidal plates [27], axisymmetric bending of FG-GRC circular and annular plates [28], or biaxially compressed buckling and postbuckling behaviors of FG-GRC plates [29].

Along with these works reporting on the fascinating stiffening capacity of GNPs, there also exist some studies in the literature that report no improvements or even reductions in the overall mechanical properties [30, 31]. One of the main reasons of these discrepancies is the appearance of non-uniform spatial distributions of nanofillers. Due to the electronic configuration of carbon-based nanoparticles as well as their high specific surface area, and therefore, large van der Waals (vdW) attraction forces [32–34], both GNPs and CNTs tend to agglomerate. A noticeable contribution in this respect was the work by Shi *et al.* [35] who introduced a two-parameter agglomeration model to estimate the macroscopic elastic moduli of CNT-reinforced polymer composites. That approach consists of considering the agglomerates as ellipsoidal inclusions so that one can conduct the homogenization process in two separate steps. Their results demonstrated substantial decreases in the elastic moduli of the composites, what supports the widespread thought of agglomeration as microstructure defects. Numerous research works can be found in the literature on the application of the two-parameter agglomeration model for the analysis of heterogeneous CNT distributions [36–40]. Also, the two-parameter agglomeration model was utilized by Ji *et al.* [20] to investigate the agglomeration effects in GRCs. Their results highlighted the detrimental effect of agglomeration on the macroscopic mechanical behavior of the nanocomposites. Furthermore, it has been reported in the literature that individual layers of graphene undergo out-of-plane wrapping, rippling, folding, scrolling and crumpling [41–43], which can weaken the effective behavior of GRCs. In this line, Ji *et al.* [20] extended the Mori-Tanaka micromechanics approach to account for restacking of graphene sheets forming multi-layered graphite. Likewise, their results reported reductions in the overall elastic moduli with increasing number of graphene sheets restacked into graphite platelets.

In this paper, the bending and vibrational behaviors of FG-GRC polymer plates are investigated. The Mori-Tanaka homogenization scheme is utilized to estimate the macroscopic elastic properties of the composites. The numerical simulations are conducted with a self-developed First-order Shear Deformation (FSD) shell finite element code. Detailed parametric analyses are presented to assess the benefits, from a mechanical perspective, of graphene compared to CNTs. In addition, the two-parameter agglomeration model is adopted to estimate the agglomeration effects. Finally, the effects of restacking of graphene sheets on the bending and free-vibration behaviors of composite plates are also analyzed.

This paper is organized as follows: Section 2 presents the composite plates analyzed in this study. Section 3 overviews the micromechanics homogenization of the elastic moduli of FG-GRC polymers, for both fully aligned and randomly oriented filler configurations. Section 4 introduces the consideration of some limiting factors of the load bearing capacity of polymer nanocomposites, including agglomeration effects and restacking of graphene

sheets. Section 5 outlines the finite element formulation of FG-GRC plates. Section 6 presents the numerical results and discussion and, finally, Section 7 concludes the paper and summarizes the main findings.

2. FG-GRC polymer plates

Figure 1 shows the polymer nanocomposite plates studied in this paper, with length a, width b, and thickness t. An atom thick graphene sheet is comprised of a two-dimensional (2D) hexagonal network of covalently bonded carbon atoms (see Fig. 2). In order to define the graphene microstructure, a local coordinate system x_1'-x_2'-x_3' is set up as shown in Fig. 2(a). Thence, GNPs lay on the x_1'-x_2' planes with x_3'-axis normal to their surface. In the case of fully aligned GRC plates, GNPs are assumed to be arranged in the global x_1-x_2 plane that is parallel to the mid-plane of the plate as sketched in Fig. 1.

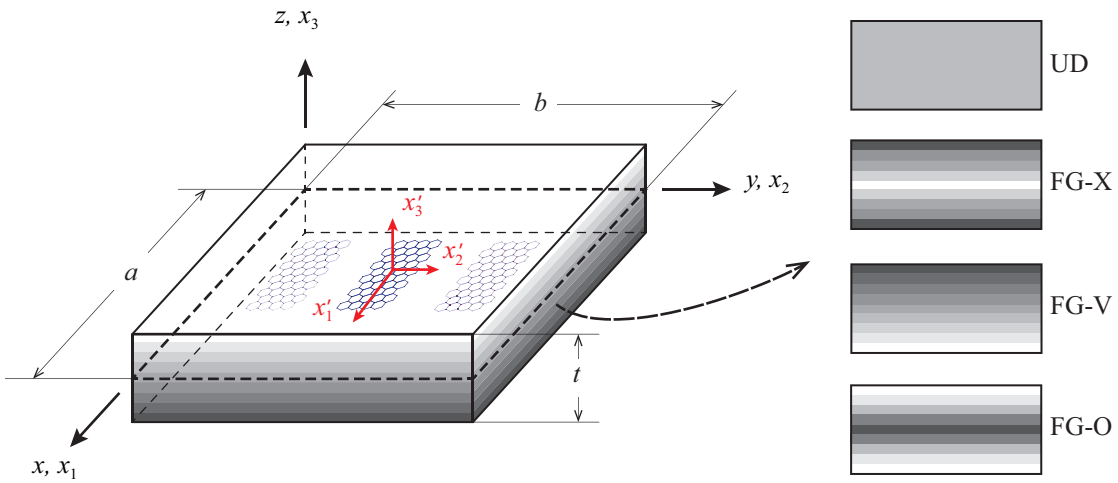

Figure 1: Geometry and coordinate system of FG-GRC polymer plates.

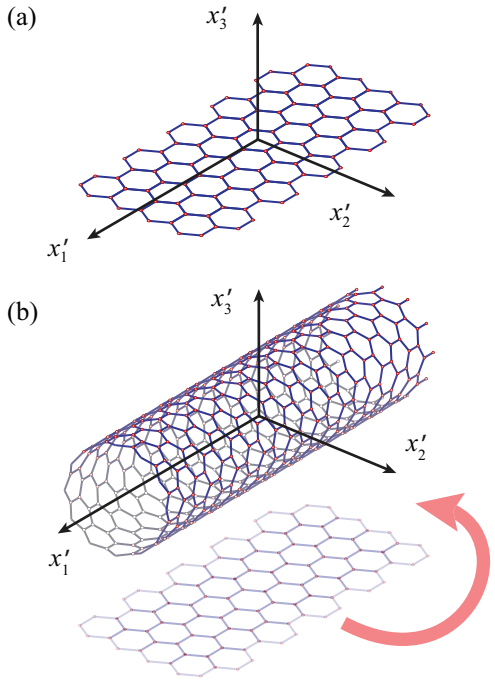

Figure 2: Coordinate system for a single graphene sheet (a) and a carbon nanotube (b).

In addition, GNPs are defined functionally graded across the thickness of the plate by four different distributions, namely UD, FG-V, FG-O and FG-X. UD represents the uniform distribution, whilst FG-V, FG-O and FG-X

are power law distributions of GNPs across the thickness. According to these distributions, the GNP volume fraction $f_r(z)$ is defined as a function of $z \in [-t/2, t/2]$ as:

$$f_r(z) = f_r^* \qquad \text{(UD)} \tag{1a}$$

$$f_r(z) = \left(\frac{2\,|z|}{t}\right)^k (k+1) f_r^* \qquad \text{(FG-X)} \tag{1b}$$

$$f_r(z) = \left(\frac{t+2z}{2t}\right)^k (k+1) f_r^* \qquad \text{(FG-V)} \tag{1c}$$

$$f_r(z) = \left(\frac{t-2\,|z|}{t}\right)^k (k+1) f_r^* \qquad \text{(FG-O)} \tag{1d}$$

being f_r^* the total volume fraction of GNPs, and k a power-law index. The filler distribution along the thickness direction is depicted in Fig. 3 for power-law indexes of 0.5, 0.7, 1, 1.3 and 1.8. It can be noted that linear distributions are obtained if the grading index is set to one. In practice, the concentration of fillers f_r is often expressed in terms of weight fraction wt as follows:

$$f_r = \frac{wt}{wt + (\rho_r/\rho_m)\,(1 - wt)} \tag{2}$$

where ρ_r and ρ_m stand for the mass density of the fillers and the matrix material. Hence, the overall density of the composite can be computed by the rule of mixtures as $\rho = f_r\rho_r + f_m\rho_m$. Finally, the volume fraction of the matrix is $f_m = 1 - f_r$.

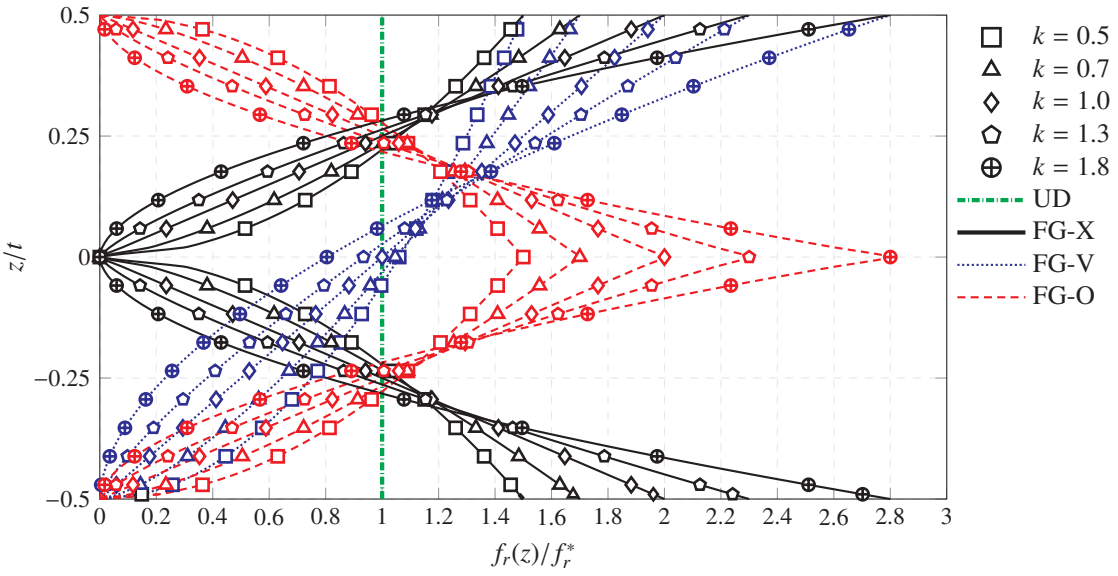

Figure 3: Variations of GNP volume fraction along the thickness direction for UD, FG-X, FG-V and FG-O profiles.

3. Micromechanics prediction of the effective elastic moduli of GRCs

This section briefly overviews the micromechanics prediction of the elastic moduli of GRCs. The Mori-Tanaka (MT) homogenization framework is considered and both fully aligned and randomly oriented filler configurations are studied.

3.1. Effective elastic properties of fully aligned nanoinclusions

Let V denote the Representative Volume Element (RVE) of an isotropic polymer matrix doped with a sufficient number of fillers in such a way that the overall properties of the composite are statistically represented [44]. In spite of the fact that a widely-accepted definition of the elastic moduli of graphene is still lacking in the literature, most studies agree to consider graphene as transversely isotropic inclusions dispersed throughout the matrix. In conjunction with Hill's notation, the constitutive matrix for inclusions with transversely isotropic properties in the local coordinate system $x_1' - x_2' - x_3'$ (x_3' the axis of material symmetry) takes the form:

$$\mathbf{C}'_r = \begin{bmatrix} k_r + m_r & k_r - m_r & l_r & 0 & 0 & 0 \\ k_r - m_r & k_r + m_r & l_r & 0 & 0 & 0 \\ l_r & l_r & n_r & 0 & 0 & 0 \\ 0 & 0 & 0 & p_r & 0 & 0 \\ 0 & 0 & 0 & 0 & p_r & 0 \\ 0 & 0 & 0 & 0 & 0 & m_r \end{bmatrix} \tag{3}$$

where k_r, l_r, m_r, n_r and p_r are Hill's elastic moduli [45]; k_r is the plane-strain bulk modulus under lateral dilatation in the $x'_1 - x'_2$ plane, n_r is the uniaxial tension modulus in x'_3 direction, l_r is the associated cross modulus, m_r and p_r are the shear moduli in the $x'_1 - x'_2$ and $x'_1 - x'_3$ planes, respectively. Throughout this work, the superscripts "r" and "m" refer the corresponding quantity to the inclusion and matrix occupied portions of V. With this convention, and assuming perfect bonding between phases, the relations between the total average strain and stress tensors in the RVE, $\overline{\boldsymbol{\varepsilon}}$ and $\overline{\boldsymbol{\sigma}}$, respectively, are defined by the rule of mixtures as follows:

$$\overline{\boldsymbol{\varepsilon}} = f_m \overline{\boldsymbol{\varepsilon}}^m + f_r \overline{\boldsymbol{\varepsilon}}^r \tag{4}$$

$$\overline{\boldsymbol{\sigma}} = f_m \overline{\boldsymbol{\sigma}}^m + f_r \overline{\boldsymbol{\sigma}}^r \tag{5}$$

here, $\overline{\boldsymbol{\varepsilon}}^m$ and $\overline{\boldsymbol{\sigma}}^m$ are the average strain and stress in the matrix, and $\overline{\boldsymbol{\varepsilon}}^r$ and $\overline{\boldsymbol{\sigma}}^r$ are the corresponding orientation-dependent average fields in a typical inclusion. In addition, the interaction between the average inclusion strain with the corresponding average matrix strain is governed by the strain concentration tensor $\mathbf{A}$ as:

$$\overline{\boldsymbol{\varepsilon}}^r = \mathbf{A} : \overline{\boldsymbol{\varepsilon}}^m \tag{6}$$

Equations (4), (5), and (6), as well as the linear elastic constitutive laws of the phases, namely inclusion and matrix as $\overline{\boldsymbol{\sigma}}^r = \mathbf{C}_r : \overline{\boldsymbol{\varepsilon}}^r$ and $\overline{\boldsymbol{\sigma}}^m = \mathbf{C}_m : \overline{\boldsymbol{\varepsilon}}^m$, respectively, suffice to identify the overall stiffness $\mathbf{C}$ defined through $\overline{\boldsymbol{\sigma}} = \mathbf{C} : \overline{\boldsymbol{\varepsilon}}$. In the case of fully aligned fillers, the local and global coordinate systems coincide, i.e. $\mathbf{C}'_r = \mathbf{C}_r$, and the resulting overall constitutive tensor reads:

$$\mathbf{C} = \mathbf{C}_m + f_r \left[(\mathbf{C}_r - \mathbf{C}_m) : \mathbf{A} \right] \tag{7}$$

The Mori-Tanaka (MT) method [46] is one of the most commonly used homogenization approaches due to its simplicity. The MT method allows extending the theory of Eshelby [47, 48], restricted to one single inclusion embedded in a semi-infinite elastic, homogeneous and isotropic medium, to the case of a finite domain doped with multiple inhomogeneities. According to Benveniste's revision [49], the effective elastic tensor by the MT method writes:

$$\mathbf{C} = \left[f_m \mathbf{C}_m + f_r \left(\mathbf{C}_r : \mathbf{A}^{dil} \right) \right] : \left(f_m \mathbf{I} + f_r \mathbf{A}^{dil} \right)^{-1} \tag{8}$$

where $\mathbf{I}$ is the fourth rank identity tensor, and $\mathbf{A}_r^{dil}$ denotes the strain concentration tensor for the limit case of a single anisotropic ellipsoidal inhomogeneity in a dilute regime and whose expression reads:

$$\mathbf{A}^{dil} = \left[\mathbf{I} + \mathbf{S} : \mathbf{C}_m^{-1} : (\mathbf{C}_r - \mathbf{C}_m) \right]^{-1} \tag{9}$$

The Eshelby's tensor $\mathbf{S}$, well documented in Mura [50], accounts for the interaction of the mechanical strain within an isolated inclusion and the elastic surrounding medium. In order to count on a general framework for the analysis of both 2D graphene layers and 1D CNTs, and considering the high aspect ratios of both nanoinclusions, the fillers can be approximately defined as ellipsoidal inclusions as:

$$\frac{x_1^2}{a_1^2} + \frac{x_2^2}{a_2^2} + \frac{x_3^2}{a_3^2} \leq 1 \tag{10}$$

with a_1, a_2, and a_3 the semi-axes of the inclusions in the x_1, x_2 and x_3 axes. Hence, the general Eshelby's tensor is defined as:

$$S_{ijkl} = S_{jikl} = S_{ijlk}, \tag{11a}$$

$$S_{1111} = \frac{3}{8\pi(1-\nu_m)} a_1^2 I_{11} + \frac{1-2\nu_m}{8\pi(1-\nu_m)} I_1, \tag{11b}$$

$$S_{1122} = \frac{1}{8\pi(1-\nu_m)} a_2^2 I_{12} - \frac{1-2\nu_m}{8\pi(1-\nu_m)} I_1, \tag{11c}$$

$$S_{1133} = \frac{1}{8\pi(1-\nu_m)} a_3^2 I_{13} - \frac{1-2\nu_m}{8\pi(1-\nu_m)} I_1, \tag{11d}$$

$$S_{1212} = \frac{a_1^2 + a_2^2}{16\pi(1-\nu_m)} I_{12} + \frac{1-2\nu_m}{16\pi(1-\nu_m)} I_1, \tag{11e}$$

$$\Delta(s) = \sqrt{(a_1^2+s)(a_2^2+s)(a_3^2+s)} \tag{12a}$$

$$I_1 = 2\pi a_1 a_2 a_3 \int_0^\infty \frac{\mathrm{d}s}{(a_1^2+s)\Delta(s)} \tag{12b}$$

$$I_{11} = 2\pi a_1 a_2 a_3 \int_0^\infty \frac{\mathrm{d}s}{(a_1^2+s)^2\Delta(s)} \tag{12c}$$

$$I_{12} = 2\pi a_1 a_2 a_3 \int_0^\infty \frac{\mathrm{d}s}{(a_1^2+s)(a_2^2+s)\Delta(s)} \tag{12d}$$

The remaining coefficients can be found by simultaneous cyclic permutation of (1,2,3) and (a_1,a_2,a_3). The definition of the Eshelby's tensor in Voigt matrix notation writes:

$$S_{pq} = \begin{cases} S_{ijkl} & \text{if} \quad p = 1,2,3 \\ 2S_{ijkl} & \text{if} \quad p = 4,5,6 \end{cases} \tag{13}$$

Finally, for practical interest, the Hill's elastic moduli of the resulting composite (k, l, m, n, p) can be expressed in terms of engineering constants as [36]:

$$E_{11} = n - \frac{l^2}{k}, \quad E_{22} = \frac{4m(k-l^2)}{k - l^2 + mn}, \tag{14}$$

$$\nu_{12} = \nu_{13} = \frac{l}{2k}, \quad G_{12} = G_{13} = p, \tag{15}$$

$$\nu_{23} = \frac{n(k-m) - l^2}{n(k+m) - l^2}, \quad G_{23} = \frac{E_{22}}{2\,(1+\nu_{23})} \tag{16}$$

where E_{11} and E_{22} denote the longitudinal and transverse effective Young's moduli, G_{12}, G_{13}, ν_{12} and ν_{12} are the out-of-plane shear moduli and Poisson's ratios, and G_{23} and ν_{23} denote the in-plane shear modulus and Poisson's ratio.

3.2. Effective elastic properties of randomly oriented nanoinclusions

In order to describe the orientation of a general ellipsoidal inclusion, three Euler angles (θ, ϕ, ψ) are defined as illustrated in Fig. 4. Due to the high number of fillers contained in the RVE, the description of their orientation field is of statistical nature. Hence, the probability of a filler lying in an infinitesimal range of angles $[\theta, \theta + \mathrm{d}\theta] \times [\phi, \phi + \mathrm{d}\phi] \times [\psi, \psi + \mathrm{d}\psi]$ is given by $\Omega(\theta, \phi, \psi) \sin(\theta) \mathrm{d}\theta \mathrm{d}\phi \mathrm{d}\psi$, with $\Omega(\theta, \phi, \psi)$ being the so-called Orientation Distribution Function (ODF). Any ODF must satisfy the following normalization condition:

$$\int_0^{2\pi} \int_0^{2\pi} \int_0^{\pi/2} \Omega(\theta, \phi, \psi) \sin(\theta) \mathrm{d}\theta \mathrm{d}\phi \mathrm{d}\psi = 1 \tag{17}$$

The integration of any ODF-weighted tensor $F(\theta, \phi, \psi)$ over all possible orientations in the Euler space, also referred to as the orientational average of F, $\langle F \rangle$, is defined through:

$$\langle F \rangle = \int_0^{2\pi} \int_0^{2\pi} \int_0^{\pi/2} F(\theta, \phi, \psi) \Omega(\theta, \phi, \psi) \sin(\theta) \mathrm{d}\theta \mathrm{d}\phi \mathrm{d}\psi \tag{18}$$

The tensor F' in the local coordinate system $x_1' - x_2' - x_3'$ is related to the global coordinate system using $F_{ijkl} = a_{ip} a_{jq} a_{kr} a_{ls} F'_{pqrs}$, where $\mathbf{a}$ is the transformation matrix consisting of θ, ϕ, and ψ rotation angles. If the fillers are completely randomly oriented, the ODF is $\Omega(\theta, \phi, \psi) = 1/4\pi^2$. According to the MT method, the overall constitutive tensor is defined as:

$$\mathbf{C} = \left(f_m \mathbf{C}_m + f_r \left\langle \mathbf{C}_r(\theta, \phi, \psi) \mathbf{A}^{dil}(\theta, \phi, \psi) \right\rangle \right) : \left(f_r \mathbf{I} + f_r \left\langle \mathbf{A}^{dil}(\theta, \phi, \psi) \right\rangle \right)^{-1} \tag{19}$$

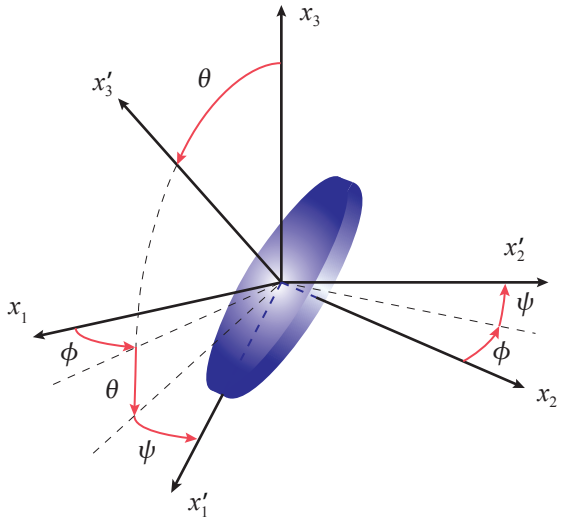

Figure 4: Schematic illustrating the Euler angles (θ, ϕ, ψ) defining the orientation of a platelet inclusion.

4. Factors limiting the load bearing capacity

In this section, factors limiting the load bearing capacity are incorporated in the previously presented micromechanics approach, including agglomeration and restacking of graphene sheets.

4.1. Agglomeration effects

A critical phenomenon to be taken into consideration for the simulation of GRCs is the appearance of non-uniform spatial distributions of nanoinclusions. The difficulty in obtaining good fiber dispersions is related to the circumstance that nanofillers tend to agglomerate in bundles. This effect is attributed to the electronic configuration of carbon-based nanoparticles and their high specific surface area which increases the vdW attraction forces between fillers [32–34]. It is extensively reported in the literature that bundles can substantially decrease the overall mechanical properties of the composites. In this paper, a two-parameter agglomeration model is adopted to model the effective mechanical properties of non-uniform distributions of fillers. This approach differentiates two regions, one with high filler concentration, corresponding to spherical clusters, and another with low filler concentration, that is the surrounding composite. Therefore, the total volume of fillers, V_r, dispersed in V can be divided into the following two parts:

$$V_r = V_r^{bundles} + V_r^m \tag{20}$$

where $V_r^{bundles}$ and V_r^m denote the volumes of fillers dispersed in the bundles and in the matrix, respectively. In order to characterize the agglomeration effects, Shi *et al.* [35] introduced two parameters, ξ and ζ, as follows:

$$\xi = \frac{V_{bundles}}{V}, \quad \zeta = \frac{V_r^{bundles}}{V_r} \tag{21}$$

where $V_{bundles}$ is the volume occupied by the bundles. The agglomeration parameter ξ represents the volume ratio of bundles with respect to the total volume V. On the other hand, ζ stands for the volume ratio of fillers within the bundles with respect to the total volume V. This pair of parameters unequivocally determines the agglomeration scheme as outlined in Fig. 5 (a). After some manipulations, the filler volume fractions in the bundles and the surrounding composite, c_1 and c_2, respectively, can be expressed as:

$$c_1 = f_r \frac{\zeta}{\xi}, \quad c_2 = f_r \frac{1-\zeta}{1-\xi} \tag{22}$$

It can be extracted from Eq. (22) that $\zeta \geq \xi$ must be fulfilled in order to impose a higher filler concentration in the clusters. The limit case $\zeta = \xi$ represents an uniform distribution of fillers, whilst the heterogeneity degree grows for larger values of ζ up the limit case $\zeta = \min(1, \xi/f_r)$. Hence, the homogenization process can be carried out in two steps. Firstly, the overall constitutive tensor of the inclusions, $\mathbf{C}^{\text{in}}$, and the surrounding composite, $\mathbf{C}^{\text{out}}$, are obtained with polymer as matrix and nanoparticles as reinforcing phase with volume fractions c_1 and c_2, respectively. Secondly, the effective constitutive tensor of the composite, $\mathbf{C}^*$, is computed considering the

surrounding composite as matrix material and bundles as inclusions. On this basis, the micromechanics approach of Eq. (8) can be extended to account for agglomeration. Moreover, the consideration of agglomeration effects can be readily extended in the realm of functionally graded materials as sketched in Fig. 5 (b).

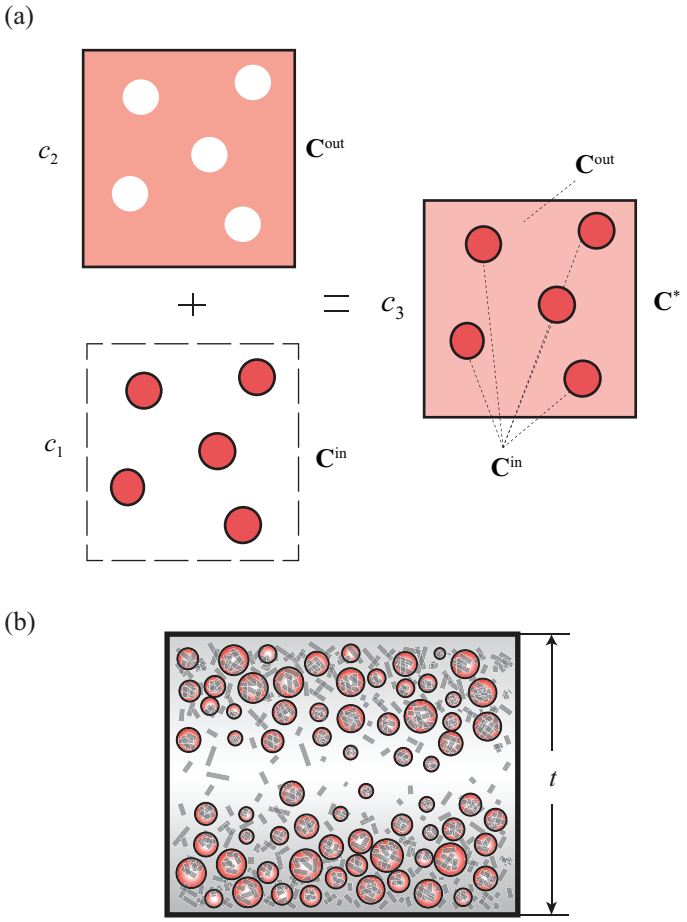

Figure 5: Schematic representation of the two parameter agglomeration model (a) and of a functionally graded material with agglomerates (b).

4.2. Restacking of graphene sheets

In practical nanocomposites, 2D graphene sheets have a tendency to stack up and form multi-layered graphite due to the steric effect and the vdW interaction between different sheets. The shape of graphite influences the stiffening effect due to its dominance in the Eshelby's tensor. We inspect the situation where GNPs stack up in the shape of ellipsoids with two semi-major axes equal in length, i.e. $a_1 = a_2$, and a semi-minor axis a_3 defined by the aspect ratio a_3/a_1 representing the thickness of the resulting restacked graphene sheets, as shown in Fig. 6. On this basis, the Eshelby's tensor can be reckoned by Eqs. (11) and (12). When tensile loads are transferred to the stacked graphene sheets, vdW bonding between layers is likely to fail before graphitic carbon-carbon bonding, leading to further exfoliation of the particle. For this reason, the in-plane elastic moduli remain similar to those of graphene sheets although the out-of plane modulus approximates that of graphite, as shown in the MM simulations of Chou *et al.* [51].

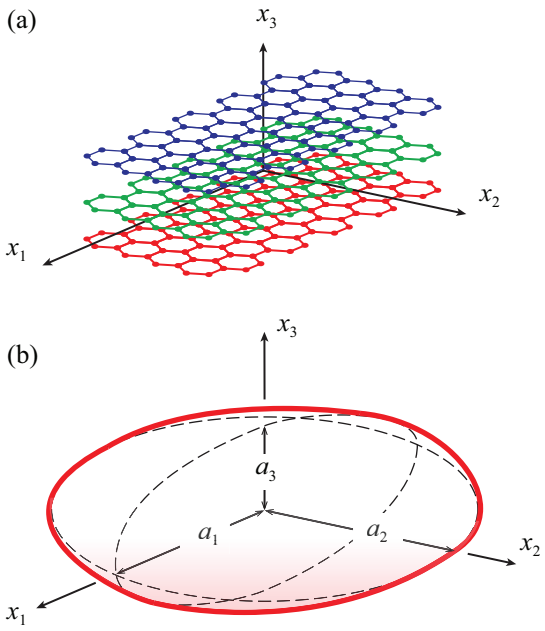

Figure 6: Schematic representation of restacking of graphene sheets forming multi-layered graphite (a) and equivalent ellipsoid (b).

Fig. 7 shows the normalized longitudinal effective moduli $E_{\|}/E_m$ of a composite reinforced by fully aligned restacked graphene sheets as a function of the ratio of semi-axes a_3/a_1. It is observed in this figure that small values of a_3/a_1, that is a low restacking degree, yield optimum stiffening properties. Conversely, when the aspect ratio a_3/a_1 increases up to E-2, the stiffening effect is seriously diminished.

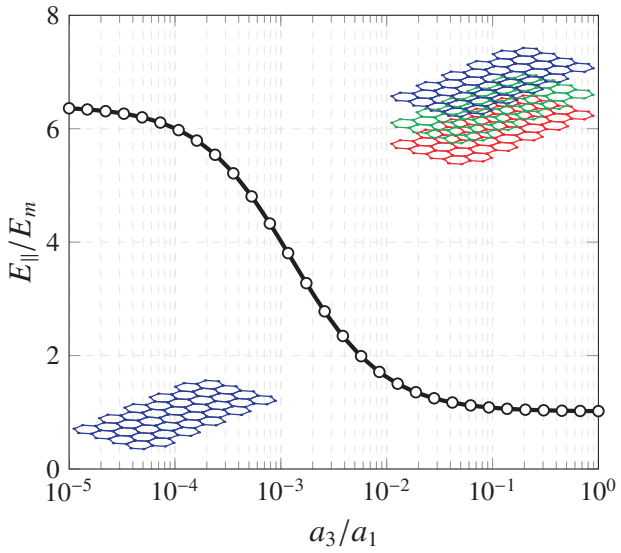

Figure 7: Normalized effective longitudinal moduli of a composite reinforced by fully aligned restacked graphene sheets (E_m=1.9 GPa, ν_m=0.3, k_r=620.0 GPa, l_r=15.0 GPa, n_r=36.5 GPa, m_r=440.0 GPa, p_r=4.0 GPa).

5. Finite element formulation

Considering moderately thick GRC polymer plates, the First order Shear Deformation Theory (FSDT) is employed to account for the displacement field $\{u, v, w\}^{\mathrm{T}}$ within a plate domain, according to the displacements and rotations of the mid-plane of the plate:

$$\begin{Bmatrix} u(x,y,z) \\ v(x,y,z) \\ w(x,y,z) \end{Bmatrix} = \begin{Bmatrix} u_o(x,y) \\ v_o(x,y) \\ w_o(x,y) \end{Bmatrix} + z \begin{Bmatrix} \varphi_x(x,y) \\ \varphi_y(x,y) \\ 0 \end{Bmatrix} \tag{23}$$

where u_o, v_o and w_o denote the respective translation displacements of a point at the mid-plane of the plate in x, y and z directions; φ_x and φ_y stand for rotations of a transverse normal about the positive y and negative x axes, respectively. Hence, the in-plane and transverse shear strains write:

$$\begin{Bmatrix}\varepsilon_{xx}\\ \varepsilon_{yy}\\ \varepsilon_{xy}\end{Bmatrix} = \boldsymbol{\varepsilon}_0 + z\mathbf{K}, \quad \begin{Bmatrix}\gamma_{yz}\\ \gamma_{xz}\end{Bmatrix} = \boldsymbol{\gamma}_0 \tag{24}$$

where:

$$\boldsymbol{\varepsilon}_0 = \begin{Bmatrix} \frac{\partial u_o}{\partial x} \\ \frac{\partial v_o}{\partial y} \\ \frac{\partial u_o}{\partial y} + \frac{\partial v_o}{\partial x} \end{Bmatrix}, \quad \mathbf{K} = \begin{Bmatrix} \frac{\partial \varphi_x}{\partial x} \\ \frac{\partial \varphi_y}{\partial y} \\ \frac{\partial \varphi_x}{\partial y} + \frac{\partial \varphi_y}{\partial x} \end{Bmatrix}, \quad \boldsymbol{\gamma}_0 = \begin{Bmatrix} \varphi_y + \frac{\partial w_o}{\partial y} \\ \varphi_x + \frac{\partial w_o}{\partial x} \end{Bmatrix} \tag{25}$$

In order to implement the constitutive equations of FG-GRCs into the modeling, let us note the constitutive equations in Voigt's notation as follows:

$$\begin{bmatrix}\sigma_{xx}\\ \sigma_{yy}\\ \sigma_{xy}\\ \sigma_{yz}\\ \sigma_{xz}\end{bmatrix} = \begin{bmatrix} Q_{11}(z) & Q_{12}(z) & 0 & 0 & 0 \\ Q_{12}(z) & Q_{22}(z) & 0 & 0 & 0 \\ 0 & 0 & Q_{66}(z) & 0 & 0 \\ 0 & 0 & 0 & Q_{44}(z) & 0 \\ 0 & 0 & 0 & 0 & Q_{55}(z) \end{bmatrix} \cdot \begin{bmatrix}\varepsilon_{xx}\\ \varepsilon_{yy}\\ \varepsilon_{xy}\\ \varepsilon_{yz}\\ \varepsilon_{xz}\end{bmatrix} \tag{26}$$

$$\begin{aligned} &Q_{11} = \tfrac{E_{11}}{1-\nu_{12}\nu_{21}}, \quad Q_{22} = \tfrac{E_{22}}{1-\nu_{12}\nu_{21}}, \quad Q_{12} = \tfrac{\nu_{21}E_{11}}{1-\nu_{12}\nu_{21}}, \\ &Q_{66} = G_{12}, \qquad Q_{44} = G_{23}, \qquad Q_{55} = G_{13} \end{aligned} \tag{27}$$

Note that Q_{ij} varies with z according to the grading profile of the fillers across the thickness. Thus, the components of the extensional stiffness, $\mathbf{C}_\mathrm{E}$, bending-extension-coupling stiffness, $\mathbf{C}_\mathrm{C}$, bending stiffness, $\mathbf{C}_\mathrm{B}$, and transverse shear stiffness, $\mathbf{C}_\mathrm{S}$, are defined by the following integrals:

$$\begin{aligned} &(C_\mathrm{E}^{ij}, C_\mathrm{C}^{ij}, C_\mathrm{B}^{ij}) = \textstyle\int_{-t/2}^{t/2} Q_{ij}(z)\cdot(1, z, z^2)\mathrm{d}z \quad (i,j = 1,2,6), \\ &C_\mathrm{S}^{ij} = \tfrac{1}{ks}\textstyle\int_{-t/2}^{t/2} Q_{ij}(z)\mathrm{d}z \quad (i,j = 4,5) \end{aligned} \tag{28}$$

where ks denotes the transverse shear correction factor for two-phase FG materials, given by Efraim and Eisenberg [52] as:

$$ks = \frac{6 - (\nu_{12}^r f_r + \nu^m V_m)}{5} \tag{29}$$

The generalized displacements at any point within an element domain Ω^e are independently interpolated using the same shape functions as:

$$\begin{aligned} &(u_o, v_o, w_o) = \textstyle\sum_{i=1}^n N_i(\xi,\eta)(u_i, v_i, w_i), \\ &(\varphi_x, \varphi_y) = \textstyle\sum_{i=1}^n N_i(\xi,\eta)(\varphi_{xi}, \varphi_{yi}) \end{aligned} \tag{30}$$

where $N_i(\xi,\eta)$ are the shape functions of a bilinear four-noded Q4 element. Following the standard procedure, the finite element equations of composite plates subjected to external loading can be expressed as:

$$\mathbf{Kd} = \mathbf{F} \tag{31}$$

where $\mathbf{K}$, $\mathbf{d}$, and $\mathbf{F}$ are the global stiffness matrix, nodal displacements and load vector, respectively. The global stiffness matrix $\mathbf{K}$ is computed by assembling the element stiffness matrix $\mathbf{K}^\mathrm{e}$ given by:

$$\mathbf{K}^\mathrm{e} = \mathbf{K}_\mathrm{E}^\mathrm{e} + \mathbf{K}_\mathrm{B}^\mathrm{e} + \mathbf{K}_\mathrm{S}^\mathrm{e} \tag{32}$$

where $\mathbf{K}_\mathrm{E}^\mathrm{e}$, $\mathbf{K}_\mathrm{B}^\mathrm{e}$ and $\mathbf{K}_\mathrm{S}^\mathrm{e}$ stand for extensional, bending and shear element stiffness matrices, respectively, and are computed as follows:

$$\mathbf{K}_\mathrm{E}^\mathrm{e} = \int_{\Omega^\mathrm{e}} (\mathbf{B}_\mathrm{m})^\mathrm{T}\, \mathbf{C}_\mathrm{E}\mathbf{B}_\mathrm{m}\mathrm{d}\Omega + \int_{\Omega^\mathrm{e}} (\mathbf{B}_\mathrm{b})^\mathrm{T}\, \mathbf{C}_\mathrm{C}\mathbf{B}_\mathrm{m}\mathrm{d}\Omega \tag{33}$$

$$\mathbf{K}_\mathrm{B}^\mathrm{e} = \int_{\Omega^\mathrm{e}} (\mathbf{B}_\mathrm{b})^\mathrm{T}\, \mathbf{C}_\mathrm{B}\mathbf{B}_\mathrm{b}\mathrm{d}\Omega + \int_{\Omega^\mathrm{e}} (\mathbf{B}_\mathrm{m})^\mathrm{T}\, \mathbf{C}_\mathrm{C}\mathbf{B}_\mathrm{b}\mathrm{d}\Omega \tag{34}$$

$$\mathbf{K}_{\mathrm{S}}^{\mathrm{e}} = \int_{\Omega^{\mathrm{e}}} (\mathbf{B}_{\mathrm{s}})^{\mathrm{T}}\, \mathbf{C}_{\mathrm{S}} \mathbf{B}_{\mathrm{s}} \mathrm{d}\Omega \tag{35}$$

$$\mathbf{B}_{\mathrm{m}} = \begin{bmatrix} N_{i,x} & 0 & 0 & 0 & 0 \\ 0 & N_{i,y} & 0 & 0 & 0 \\ N_{i,y} & N_{i,x} & 0 & 0 & 0 \end{bmatrix}, \quad \mathbf{B}_{\mathrm{b}} = \begin{bmatrix} 0 & 0 & 0 & N_{i,x} & 0 \\ 0 & 0 & 0 & 0 & N_{i,y} \\ 0 & 0 & 0 & N_{i,y} & N_{i,x} \end{bmatrix} \tag{36}$$

$$\mathbf{B}_{\mathrm{s}} = \begin{bmatrix} 0 & 0 & N_{i,y} & 0 & N_i \\ 0 & 0 & N_{i,x} & N_i & 0 \end{bmatrix} \tag{37}$$

The load vector of the element, $\mathbf{F}^{\mathrm{e}}$, is computed as:

$$\mathbf{F}^{\mathrm{e}} = \int_{\Omega^{\mathrm{e}}} [N^{\mathrm{e}}]\, q_o \mathrm{d}\Omega \tag{38}$$

where q_o is the transverse load over the element.

In a free vibration analysis, the composite plate is assumed to undergo a harmonic motion and the dynamic properties, mode shapes Φ and frequencies ω, can be obtained by solving the eigenvalue equations:

$$\left(\mathbf{K} - \omega_i^2 \mathbf{M}\right) \Phi_i = 0 \tag{39}$$

where the global mass matrix $\mathbf{M}$ is computed by assembling the element mass matrices given by:

$$\mathbf{M}^{\mathrm{e}} = \int_{\Omega^{\mathrm{e}}} [N^{\mathrm{e}}]^{\mathrm{T}}\, [\boldsymbol{\rho}]\, [N^{\mathrm{e}}]\, \mathrm{d}\Omega \tag{40}$$

where

$$[\boldsymbol{\rho}] = \begin{bmatrix} I_0 & 0 & 0 & I_1 & 0 \\ 0 & I_0 & 0 & 0 & I_1 \\ 0 & 0 & I_0 & 0 & 0 \\ I_1 & 0 & 0 & I_2 & 0 \\ 0 & I_1 & 0 & 0 & I_2 \end{bmatrix} \tag{41}$$

in which I_0, I_1 and I_2 are the normal, coupled normal-rotary and rotary inertial coefficients, respectively, and defined by:

$$(I_0, I_1, I_2) = \int_{-h/2}^{h/2} \rho(z) \left(1, z, z^2\right) \mathrm{d}z \tag{42}$$

Let us note that the mass density $\rho(z)$ in the latter equation varies across the thickness according to the functionally grading of the fillers.

6. Numerical results

In this section, detailed parametric analyses of the bending and vibrational behavior of FG-GRC polymer plates are presented. According to the geometrical definition presented in Fig. 1, square plates $a/b = 1$ with thickness-to-width ratio t=a/50 are utilized for illustrative purposes unless otherwise indicated. The boundary conditions at any simply supported (S) or clamped (C) edge can be defined as follows:

$$\begin{cases} u_s = w = \varphi_s = 0 \Leftarrow \text{Simply supported edge (S)} \\ u_n = u_s = w = \varphi_n = \varphi_s = 0 \Leftarrow \text{Clamped edge (C)} \end{cases} \tag{43}$$

with u and φ standing for translation and rotational degrees of freedom, respectively. Subscripts n and s denote the normal and tangential directions, respectively. The various non-dimensional parameters used throughout this section are defined as:

$$\text{Frequency parameter} : \lambda = \omega \frac{b^2}{\pi^2} \sqrt{\frac{\rho^m t}{D}}, \tag{44a}$$

$$\text{Central deflection} : \bar{w} = \frac{w_o}{t}, \tag{44b}$$

$$\text{Central axial stress} : \bar{\sigma} = \frac{\sigma \cdot t^2}{|q_o| \cdot a^2} \tag{44c}$$

where w_o stands for vertical deflection at the central point, ω the angular frequency of the composite plates, and $D = E_m t^3/12(1-\nu_m^2)$ is the flexural rigidity of the neat polymer plate.

With regard to the different constituents analyzed in this work, the elastic moduli and mass density of the different phases are summarized in Table 1. The in-plane Young's modulus and Poisson's ratio of graphene sheets have been assumed $E_{11} = 1020$ GPa and $\nu_{12} = 0.4$, respectively, in accordance with Lee *et al.* [53] and Reddy *et al.* [54]. The out-of-plane modulus E_{33} and the shear modulus G_{13} are assumed to be 100 times the in-plane modulus, while the Poisson's ratio ν_{31} is taken as 1% of ν_{12}, i.e. $E_{33} = G_{13} = 102000$ GPa and ν_{31}=0.004 [20]. Hence, the stiffness tensor for graphene sheet inclusions can be noted as $\mathbf{C}_r^{graphene}$=$(2k_r, l_r, n_r, 2m_r, 2p_r)$ = $(1700, 6.8, 102000, 738, 204000)$ GPa. With regard to restacked graphene sheets, according to the MM simulations of Chou *et al.* [51] and the work of Ji *et al.* [20], the stiffness tensor for restacked graphene sheets is chosen as $\mathbf{C}_r^{graphite} = (1240, 15, 36.5, 880, 8)$ GPa. On the other hand, SWCNTs have been also considered for comparison purposes. According to the results by Popov *et al.* [55], the stiffness tensor for (5,5) SWCNTs is $\mathbf{C}_r^{CNT} = (60, 10, 450, 2, 2)$ GPa. Finally, the matrix material studied in this paper is polystyrene with Young's modulus $E_m = 1.9$ GPa and Poisson's ratio ν_m=0.3 so that its isotropic stiffness tensor can be noted as $\mathbf{C}_m = (3\kappa_m, 2\mu_m) = (4.75, 1.46)$, with κ_m and μ_m being the matrix's bulk and shear moduli, respectively.

Table 1: Hill's elastic moduli (k, l, n, m, p) and mass density (ρ) of constituent phases, Ref. [14, 20, 55–57].

	Graphene	**Graphite**	**CNT**		**Polystyrene**
k_r (GPa)	850.0	620.0	30.0	E_m (GPa)	1.9
l_r (GPa)	6.8	15.0	10.0	ν_m	0.3
n_r (GPa)	102000.0	36.5	450.0	ρ_m (kg/m^3)	1040
m_r (GPa)	369.0	440.0	1.0		
p_r (GPa)	102000.0	4.0	1.0		
ρ_r (kg/m^3)	2250	1060	1400		

6.1. Validation and comparison results

In order to demonstrate the validity of the present approach, convergence analyses are first conducted in order to check the stability of the finite element formulation. Then, the solutions of the proposed approach for GRCs are benchmarked against previously published results in the open literature.

6.1.1. Bending and free vibration convergence analysis of isotropic plates

In this first set of analyses, a mesh convergence study is performed for the bending and free vibration solution of square fully clamped (CCCC) isotropic plates. To this aim, square plates with dimensions $a = b = 1$ m are defined with varying thickness-to-width ratio, namely $t/a = 10^{-1}$, 10^{-2}, 10^{-3} and 10^{-4}. The transverse shear correction factor is assumed ks=6/5, and the Young's modulus and Poisson's ratio are defined as $E = 10920$ N/m^2 and $\nu = 0.3$, respectively. Firstly, the results of the mesh convergence study for the central deflection w_o under uniform transverse loading $q_o = -1$ N/m^2 are shown in Fig. 8 (a). Four sets of mesh sizes $n \times n$ (4×4, 8×8, 16×16, 24×24 and 32×32) are defined. On the other hand, Fig. 8 (b) shows the mesh convergence study for the fundamental frequency ω_1 with a mass density per unit volume $\rho = 1$ kg/m^3. Results are expressed in terms of relative error with respect to the solutions provided by a fine mesh of 64×64 elements and denoted by w_o^{exact} and ω_1^{exact} for displacements and natural frequencies, respectively. The results demonstrate the convergence of the numerical formulation and 24×24 elements are considered accurate enough for the purpose of this work. In order to prove the accuracy of the selected mesh density, the first four modes of vibration of fully simply supported (SSSS) plates are computed for two thickness-to-width ratios, namely $t/a = 0.01$ and 0.1. Results are compared against Mindlin closed-form solutions [58], and results by Liew *et al.* [59] in Table 2. The results for the selected 24×24 mesh density show excellent agreement with the reference solutions and, therefore, it is adopted throughout the subsequent calculations.

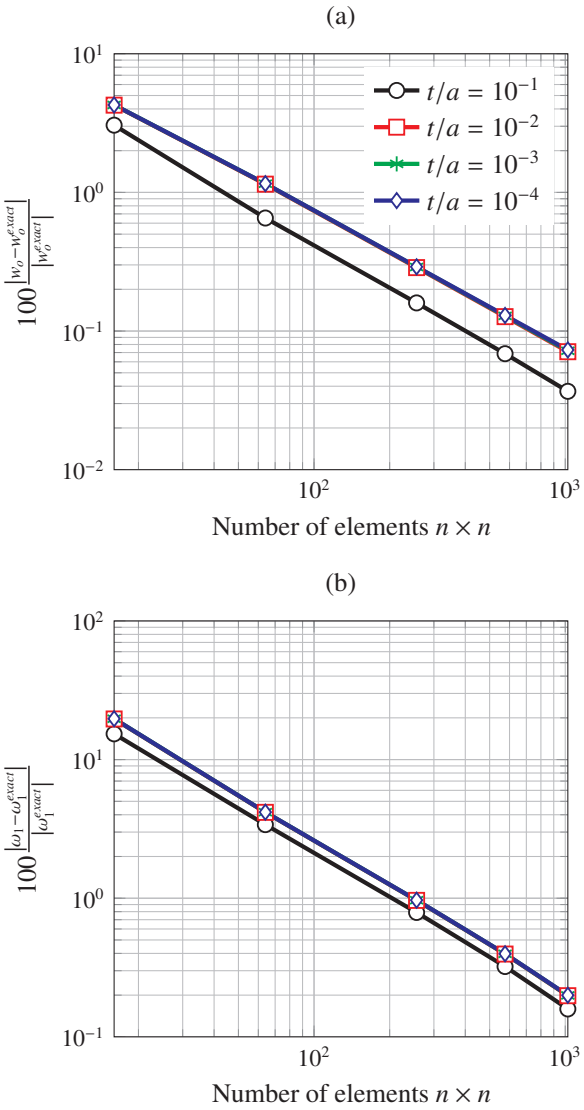

Figure 8: Mesh convergence study of the bending response (a) and fundamental frequency (b) of CCCC isotropic plates with varying thickness to width ratios t/a ($q_o = -1$ N/m^2, $a = b = 1$ m, $E = 10920$ N/m^2, $\nu = 0.3$, $\rho = 1$ kg/m^3).

Table 2: Comparison study of natural frequencies, ($\omega a \sqrt{\rho/G}$, $G = E/(2(1+\nu))$), of SSSS square isotropic plates ($a = b = 1$ m, $E = 10920$ N/m^2, $\nu = 0.3$, $\rho = 1$ kg/m^3).

t/a	Mode no.	Present	Mindlin [58]	Liew *et al.* [59]
0.1	1	0.9319	0.9300	0.9220
	2	2.2330	2.2190	2.2050
	3	2.2330	2.2190	2.2050
	4	3.4265	3.4060	3.3770
0.01	1	0.0965	0.0963	0.0961
	2	0.2422	0.2406	0.2419
	3	0.2422	0.2406	0.2419
	4	0.3877	0.3848	0.3860

6.1.2. Comparison analyses

Once the numerical approach has been shown valid for the aim of this paper, the present micromechanics framework is compared against existing results in the literature. Firstly, the theoretical estimations of the MT homogenization approach are benchmarked against the experimental results of Choudhury [60] in Fig. 9. In that work, Poly-p-phenylene benzobisthiazole (PBT)/graphene nanocomposite films with different filler contents were

fabricated and characterized. The Young's modulus and Poisson's ratio of PBT are defined as $E_m = 2.24$ GPa and $\nu_m = 0.35$, respectively. In addition, in order to further validate the present micromechanics approach, estimates provided by the modified Halpin-Tsai micromechanics model are also included. Considering graphene sheets as rectangular platelets with length l_{GNP}, width w_{GNP}, and thickness h_{GNP}, the in-plane moduli, $E_\parallel$ and $E_\perp$, write [61, 62]:

$$E_\parallel = E_m \frac{1 + \xi_L \eta_L f_r}{1 - \eta_L f_r}, \tag{45}$$

$$E_\perp = E_m \frac{1 + \xi_w \eta_w f_r}{1 - \eta_w f_r}, \tag{46}$$

$$\eta_L = \frac{E_{11}/E_m - 1}{E_{11}/E_m + \xi_L}, \tag{47}$$

$$\eta_w = \frac{E_{11}/E_m - 1}{E_{22}/E_m + \xi_w} \tag{48}$$

with ξ_L and ξ_w being parameters that characterize the geometry of GNPs as:

$$\xi_L = 2\frac{l_{GNP}}{h_{GNP}}, \tag{49}$$

$$\xi_w = 2\frac{w_{GNP}}{h_{GNP}} \tag{50}$$

In accordance with the ellipsoidal definition introduced in the MT model in Fig. 2, $l_{GNP} = a_1$, $w_{GNP} = a_2$ and $h_{GNP} = a_3$. When GNPs are arranged randomly in the x_1-x_2 plane, the composite results in a transversely isotropic material whose in-plane elastic modulus $\overline{E}_\parallel$ can be approximated by the Voigt-Reuss model [63] as:

$$\overline{E}_\parallel = \frac{3}{8}E_\parallel + \frac{5}{8}E_\perp \tag{51}$$

and the transverse modulus in the x_3-axis, $\overline{E}_\perp$, can be computed as:

$$\overline{E}_\perp = E_m \frac{1 + 2\eta_{33} f_r}{1 - \eta_{33} f_r}, \tag{52}$$

$$\eta_{33} = \frac{E_{33}/E_m - 1}{E_{33}/E_m + 2} \tag{53}$$

Finally, when GNPs are randomly oriented, the composite exhibits isotropic properties with overall elastic modulus [62]:

$$\overline{E} = 0.49E_c + 0.51\overline{E}_\perp \tag{54}$$

In addition, another Halpin-Tsai solution has been also included as proposed by Van Es [62] for disk-like platelet inclusions with modified in-plane shape factors. In this case, ξ_L and ξ_w in Eqs. (49) and (50) are modified as $\xi_L = (2/3)l_{GNP}/h_{GNP}$ and $\xi_w = (2/3)w_{GNP}/h_{GNP}$. In this case, results are denoted as H-T (B), while those obtained with the shape factors from Eqs. (49) and (50) are denoted as H-T (A). The geometrical properties of GNPs are defined as $l_{GNP} = w_{GNP} = 1.25$ μm and $h_{GNP} = 1.14$ nm [60]. It can be observed in Fig. 9 that the solutions for fillers laying on the x_1-x_2 plane, i.e. H-T (A)/(B) 2D random from Eq. (51), as well as the MT model with fully aligned configuration, largely exceed the experimental results. Since no special aligning technique was undertaken in the manufacturing process of the composites, the filler configuration presumably corresponds to a completely random orientation distribution. Accordingly, it is observed that the solutions for fully random distribution of fillers yield closer results to the experimental ones. It is also noticeable that the Halpin-Tsai solutions with modified shape factors, (B), provide very close results to MT's estimates. These results demonstrate the capability of the proposed micromechanics approach to provide quantitative estimations of the macroscopic elastic moduli of GRCs.

In order to further the comparison of the simple Halpin-Tsai model and the present micromechanics approach, Figs. 10 (a) and (b) show the estimates by both approaches for fully aligned and random configurations, respectively. In addition, the theoretical bounds of Voigt [64] and Reuss [65], as well as the Hashin-Shtrikman-Walpole bounds (HSW) [66, 67] are also included. In the case of fully aligned configurations, the MT model is shown to provide results that are coincident with the upper HSW bound. With regard to the Halpin-Tsai model, the estimates are close to the Voigt bound. In the limit case of infinite aspect ratio $a_3 \to \infty$, the Halpin-Tsai model has

been reported in the literature to coincide with the Voigt bound [62]. It is important to note that, in the case of randomly oriented distributions as in Fig. 10 (b), the load bearing capability of the fillers is reduced resulting in less stiff composites. Some results in the literature report about the superior mechanical and electrical properties of composites doped with aligned nanofillers by means of the application of high electric [68] or magnetic fields [69]. However, aligning of GNPs or CNTs remains a costly and intricate task. This type of results strengthens the importance of developing cost efficient aligning techniques for the development of high performance GRC polymers. Let us also note that, in a similar way to the previous analysis, both approaches yield close results when modified shape factors are utilized (H-T (B)), particularly for low filler contents. Finally, let us recall that it has been reported in the literature that the MT model may violate the HSW bounds [70]. Nevertheless, it can be seen in Fig. 10 (b) that for low filler contents, as typically used in practice, both approaches are comprised between these boundaries and are thus acceptable.

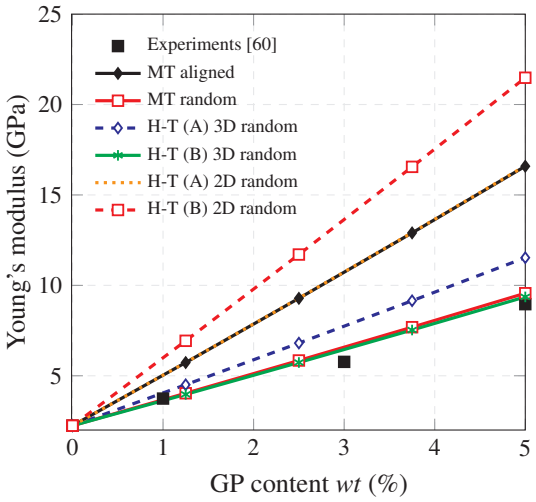

Figure 9: Comparison between the theoretical values predicted by the Halpin-Tsai and Mori-Tanaka (MT) models against the experimental Young's modulus data obtained for GNP/PBT nanocomposites by Choudhury [60]. H-T (A) and HT (B) stand for Halpin-Tsai estimates with shape factors $(\xi_L, \xi_w) = 2(l_{GNP}/h_{GNP}, w_{GNP}/h_{GNP})$ and $(\xi_L, \xi_w) = (2/3)(l_{GNP}/h_{GNP}, w_{GNP}/h_{GNP})$, respectively.

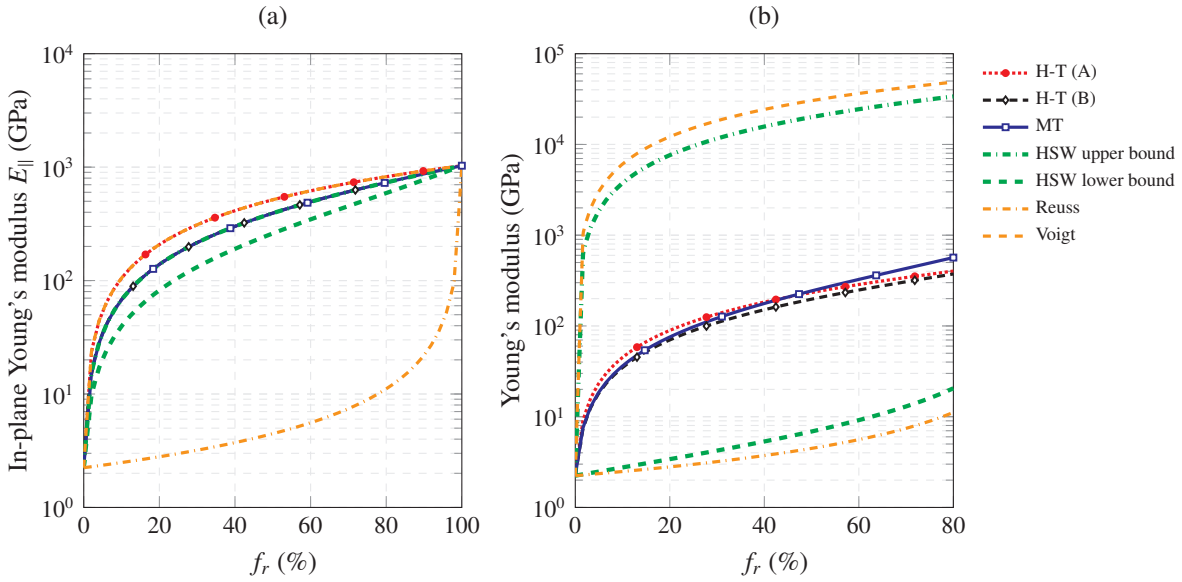

Figure 10: Halpin-Tsai and Mori-Tanaka (MT) estimates of the macroscopic elastic moduli of GNP/PBT nanocomposites for varying filler content and different filler configurations, namely (a) fully aligned and (b) randomly oriented configurations. H-T (A) and H-T (B) stand for Halpin-Tsai estimates with shape factors $(\xi_L, \xi_w) = 2(l_{GNP}/h_{GNP}, w_{GNP}/h_{GNP})$ and $(\xi_L, \xi_w) = (2/3)(l_{GNP}/h_{GNP}, w_{GNP}/h_{GNP})$, respectively.

Finally, in order to prove the validity of the modeling of FG-GRCs, the results of the present approach are compared against those published by Song *et al.* [71]. In that work, the authors studied the free and forced vibrations of FG-GRC plates by a Navier based solution and the Halpin-Tsai model. The fillers are assumed to lay on the mid-plane and are randomly oriented around the normal direction. The graphene sheets are defined as rectangular platelets with dimensions $l_{GNP} = 2.5$ μm, $w_{GNP} = 1.5$ μm and $h_{GNP} = 1.5$ nm. Epoxy is selected as matrix material with density $\rho_m = 1.20$ g/cm^3 and elastic properties $E_m = 3.0$ GPa and $\nu_m = 0.34$. GNPs are dispersed at a weight fraction of $wt = 1\%$ and functionally graded across the thickness of plates with dimensions $a = b = 0.45$ m and thickness $t = a/10$. Table 3 collects the comparison results of the natural frequencies of FG-GRC plates for UD, FG-X, FG-0 and FG-V filler grading profiles. Parameters m and n stand for the number of half-waves in the mode shapes in the x and y directions, respectively. It can be observed that the present approach provides very similar results in all the cases what demonstrates the accuracy of the present formulation. Note that the non-dimensional natural frequencies utilized in [71], $\overline{\omega} = \omega t \sqrt{\rho_m/E_m}$, are slightly different to the expression given at the beginning of this section.

Table 3: Comparison study of non-dimensional natural frequencies $\overline{\omega} = \omega t \sqrt{\rho_m/E_m}$ for simply supported FG-GRC epoxy plates ($wt = 1\%$, $a = b = 0.45$ m, $t = a/10$).

	Neat epoxy		UD		FG-0		FG-X		FG-V	
Modes (m,n)	Ref. [71]	Present	Ref. [71]	Present	Ref. [71]	Present	Ref. [71]	Present	Ref. [71]	Present
1, 1	0.058	0.058	0.122	0.121	0.102	0.097	0.138	0.141	0.112	0.117
2, 1	0.139	0.139	0.290	0.289	0.246	0.234	0.325	0.331	0.267	0.265
2, 2	0.213	0.213	0.444	0.443	0.380	0.363	0.494	0.503	0.411	0.410
3, 1	0.260	0.261	0.540	0.542	0.465	0.447	0.598	0.612	0.501	0.501
3, 2	0.325	0.326	0.677	0.678	0.586	0.564	0.745	0.760	0.630	0.625
3, 3	0.426	0.427	0.887	0.856	0.776	0.749	0.969	0.987	0.829	0.824

6.2. Parametric analyses

The results obtained by the proposed methodology have been shown to be stable and similar to those provided in the literature. Some new results are now presented. Here we analyze the static response of FG-GRC plates under uniform transverse loads, the free vibration behavior, as well as the influence of microstructure defects such as agglomeration or stacking into graphite nanoplatelets.

6.2.1. Bending of FG-GRC polymer plates

Several numerical examples are provided to investigate the bending behavior of FG-GRC polymer plates. Table 4 shows the non-dimensional central deflection $\bar{w}$ for UD, FG-V, FG-O and FG-X GRC polymer SSSS plates subjected to a uniform transverse load $q_o = -0.01$ MPa. In order to evaluate the effect of non-linear filler gradings across the thickness, different power-law indexes have been selected, namely $k = 0.5$, 1.0 and 1.8. It is noticeable that the filler content has a deep influence on the central deflection of the plates. For instance, in the case of uniform distributions, polymers doped with 1% GNP may lead to more than 85% decrease in the central deflection with respect to the pristine polymer. It is also interesting to note that the central deflections of FG-V and FG-O GRC polymer plates are larger than those of UD GRC plates, while those of the FG-X GRC polymer plates are smaller. This is because the profile of the reinforcement distribution determines the stiffness of the plates. In the FG-X case, larger power-law indexes, i.e. higher filler concentrations at top and bottom layers, lead to lower central deflections. Hence, these results support the idea of optimal distribution as the limit case of fillers concentrated at both layers, i.e. $k \to \infty$. These results also stress the main advantage of FG materials, which can tune the overall stiffness by adjusting the distribution of the fillers along the thickness direction of the plates.

Similar conclusions can be extracted from a stress analysis. Fig. 11 (a) shows the non-dimensional stress $\bar{\sigma}_{xx}$ distribution along the thickness for FG-GRC polymer plates subjected to a uniform transverse load $q_o = -0.01$ MPa with a filler volume fraction of $f_r = 0.01$. Due to the symmetric distribution (with respect to the mid-plane) of reinforcements for UD, FG-O and FG-X GRC polymer plates, the central axial stress distributions is anti-symmetric. In the case of FG-V and FG-O distributions, the axial stress is close to zero at the bottom and top layers, respectively. This is because the concentration of fillers vanishes at these points for these two distributions. The effect of non-linear filler gradings across the thickness is further investigated in Fig. 11 (b) for FG-V GRC polymer plates. Similar to the previous analysis, as k decreases the stress tends to linearize and, conversely, as k increases so does the stress at the top layer where fillers are more concentrated. It is concluded that non-linear filler distributions across the thickness, as may arise in practice as a source of uncertainty in the manufacturing process, have a substantial effect on the overall stiffness of FG-GRC polymers.

Table 4: Non-dimensional central deflection $\bar{w} = w_o/t$ in FG-GRC plates under uniform transverse loading $q_0 = 0.01$ MPa for various filler grading power-law distributions and filler contents ($a/b = 1$, $t = a/50$, SSSS).

	f_r	UD	FG-X	FG-V	FG-O
$k = 0.5$	0	1.461E+00	1.461E+00	1.461E+00	1.461E+00
	0.01	2.165E-01	1.746E-01	2.351E-01	2.945E-01
	0.05	5.113E-02	4.065E-02	5.628E-02	7.217E-02
	0.1	2.719E-02	2.179E-02	2.989E-02	3.815E-02
$k = 1.0$	0	1.461E+00	1.461E+00	1.461E+00	1.461E+00
	0.01	2.165E-01	1.526E-01	2.396E-01	3.754E-01
	0.05	5.113E-02	3.536E-02	5.852E-02	9.638E-02
	0.1	2.719E-02	1.907E-02	3.113E-02	5.096E-02
$k = 1.8$	0	1.461E+00	1.461E+00	1.461E+00	1.461E+00
	0.01	2.165E-01	1.331E-01	2.391E-01	5.028E-01
	0.05	5.113E-02	3.079E-02	6.153E-02	1.405E-01
	0.1	2.719E-02	1.673E-02	3.302E-02	7.487E-02

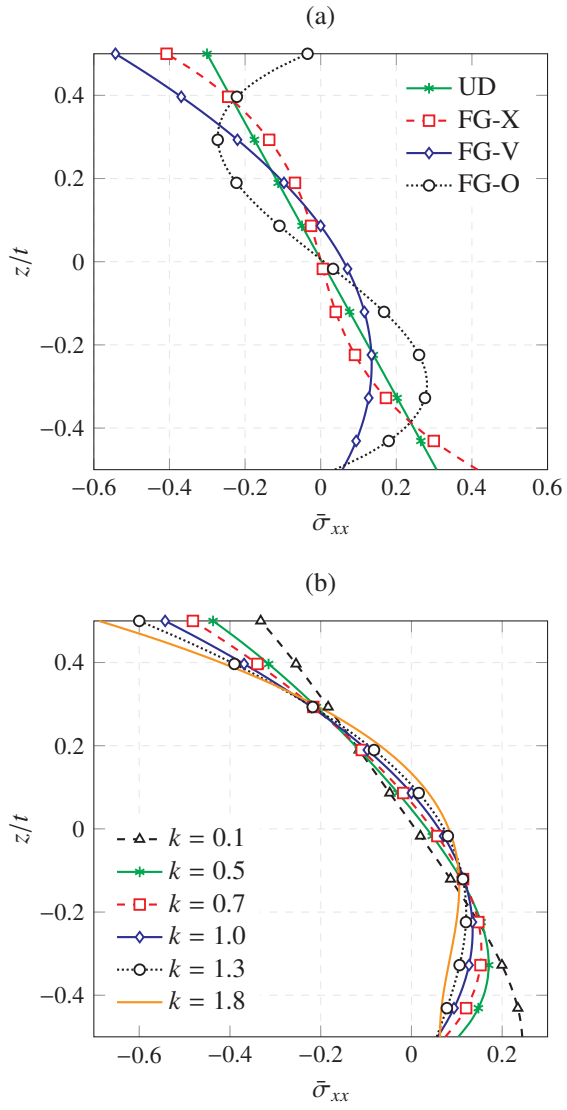

Figure 11: Non-dimensional central axial stress $\bar{\sigma}_{xx} = \frac{\sigma_{xx} t^2}{|q_o| a^2}$ in FG-GRC plates under a uniform load $q_0 = -0.1$ MPa for various linear reinforcement grading (a), and sensitivity analysis of power-law index k for FG-V reinforce grading (b) ($f_r = 0.01$, $a/b = 1$, $t = a/50$, SSSS).

6.2.2. Free vibration of FG-GRC polymer plates

The effect of the filler content on the free vibration behavior of fully aligned UD-GRC plates is analyzed in Fig. 12 for both SSSS (a) and simply supported with one free edge (SSSF) (b) boundary conditions. For comparison purposes, both GNP and SWCNT nanofillers are studied with properties defined in Table 1, corresponding to solid and dashed lines, respectively. The first three mode shapes for both nanocomposites and boundary conditions are depicted in Fig. 13. It is evidenced that the stiffening effect of GNPs overtakes that of CNTs for all the natural frequencies. For instance, the addition of graphene at a volume fraction of 0.05 rises the fundamental frequency λ_1 of the SSSS composite plates up to five times that of the neat polymer, whilst CNTs only doubles this value. Let us remark that, in the case of GRCs, the second and third natural frequencies overlap due to symmetry about $x-z$ and $y-z$ planes, in accordance with the mode shapes shown in Fig. 13. In order to further this comparison in terms of mode shapes, the MAC (Modal Assurance Criterion) matrix is depicted in Fig. 14 for SSSS boundary condition. It is observed that the MAC matrix is not a diagonal matrix and the order of appearance of characteristic mode shapes disordered due to the in-plane anisotropy of CNT-reinforced composites. For example, it is observed that the third bending mode for CNT-reinforced composites corresponds to the third mode shape, while for GNP-reinforced composites it does not appear until the sixth mode shape. This fact, together with the better dispersion of GNPs reported in the literature, supports the widespread thought of graphene as superior nanofillers for the development of high-performance composites.

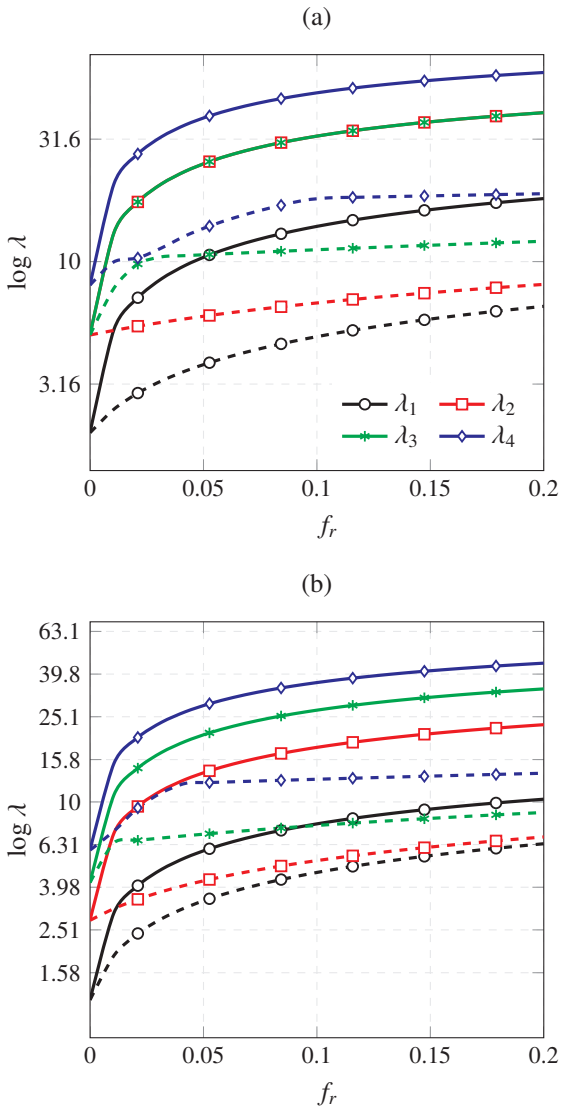

Figure 12: Non-dimensional natural frequencies versus filler volume fraction for fully aligned GNP- and CNT-reinforced composite plates, corresponding to solid and dashed lines, respectively (UD, $a/b = 1$, $t = a/50$, SSSS (a) and SSSF (b) boundary conditions).

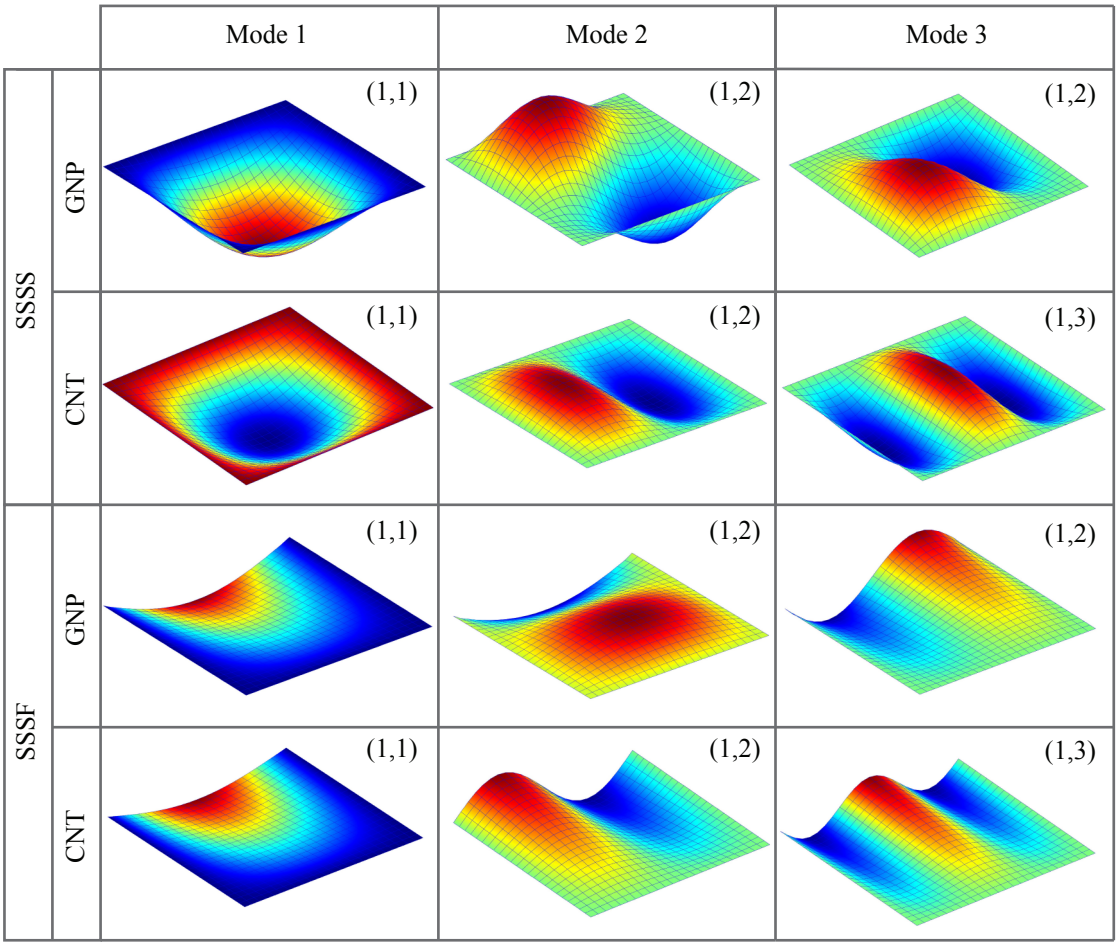

Figure 13: First three mode shapes of fully aligned GNP- and CNT-reinforced composite plates with SSSS and SSSF boundary conditions (UD, $a/b = 1$, $t = a/50$, $f_r = 0.2$).

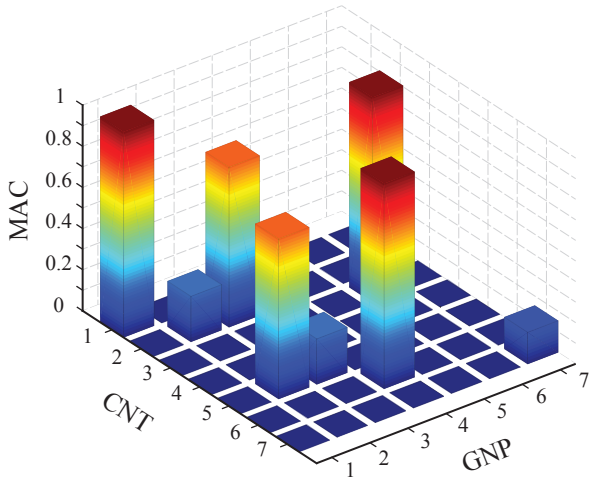

Figure 14: MAC matrix comparing the first seven mode shapes of fully aligned GNP- and CNT-reinforced composite plates with SSSS boundary condition (UD, $a/b = 1$, $t = a/50$, $f_r = 0.2$).

The comparison between the stiffening effect of GNPs and CNTs is also conducted for randomly oriented configurations as shown in Fig. 15 (a) and (b), respectively. Thence, frequency values obtained for fully aligned

nanofillers are denoted with solid lines, while those obtained for randomly oriented configurations are denoted with dashed lines. When fillers are randomly oriented, both composites exhibit isotropic properties and, thus, the second and third natural frequencies coincide. In both cases, the fundamental frequencies of plates doped with fully aligned fillers surpass those with randomly oriented fillers. However, in some other cases, e.g. fourth mode shape in Fig. 15 (b), it can be observed that the resonant frequencies are higher for random configurations. This fact is ascribed to the loss of anisotropy when fillers are randomly oriented. In order to further explain these results, the elastic moduli obtained for both nanofillers and configurations are shown in Fig. 16. Both nanofillers exhibit highly anisotropic properties when fully aligned, being the longitudinal elastic modulus, $E_{\parallel}$, several orders of magnitude higher than the transverse modulus, $E_{\perp}$. However, when nanofillers are randomly oriented, composites exhibit isotropic properties with lesser $E_{\parallel}$ but higher $E_{\perp}$ in comparison to fully aligned configurations. This fact, along with mode shapes shown in Fig. 13, gives response to the higher frequencies of some mode shapes for randomly oriented filler configurations. When the number of sine waves increases, the contribution of the transverse bending stiffness so does and, therefore, randomly oriented configurations may result in higher natural frequencies. With regard to the comparison between nanofillers, GNPs lead to much stiffer composites so that similar conclusions to the previous analysis can be extracted here. It is interesting to note that for CNT-reinforced composites, the structural behavior is considerably different for fully aligned and random orientation configurations. When CNTs are aligned in the x_2 direction, the composite exhibits transversely isotropic properties with x_2 as transverse isotropy axis. As the content of CNTs increases, the anisotropy degree of the composite plates so does and, therefore, the first mode shapes begin to be defined by a higher number of sine waves perpendicular to the filler direction. On the other hand, fully aligned GNPs are defined parallel to the mid-plane of the plate. In this case, assuming plane stress conditions, the behavior of the GRC plates is isotropic and, thus, the mode shapes do not change substantially for randomly oriented configurations.

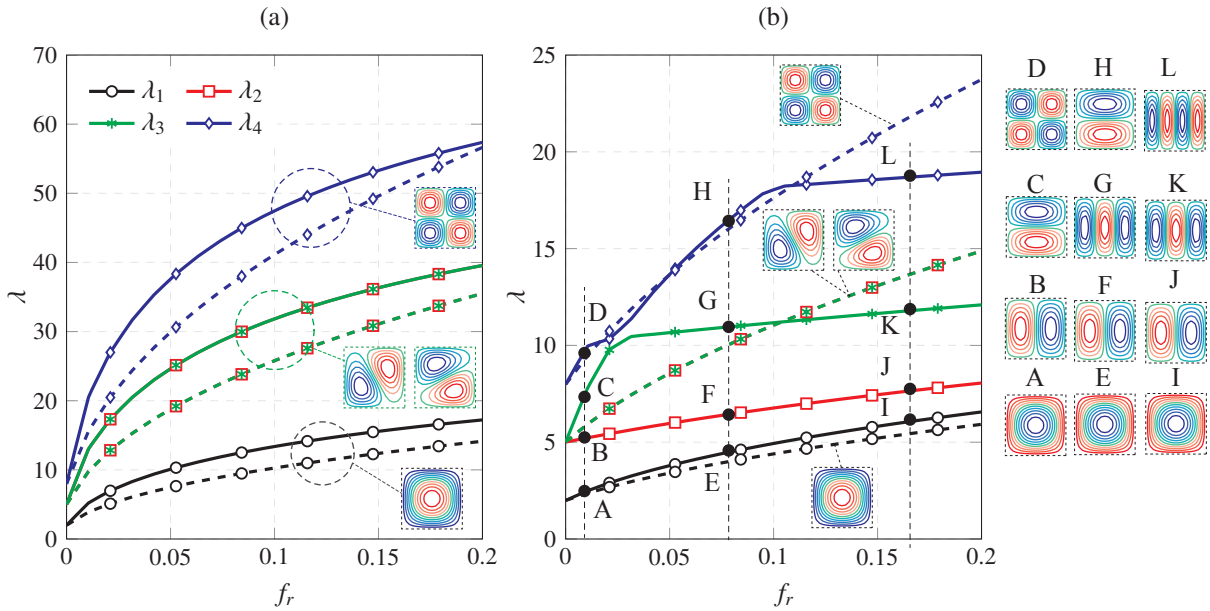

Figure 15: Non-dimensional natural frequencies for GNP- (a) and CNT-reinforced composite plates (b) versus filler volume fraction with fully aligned and randomly oriented filler configurations, corresponding to solid and dashed lines, respectively (UD, $a/b = 1$, $t = a/50$, SSSS boundary condition).

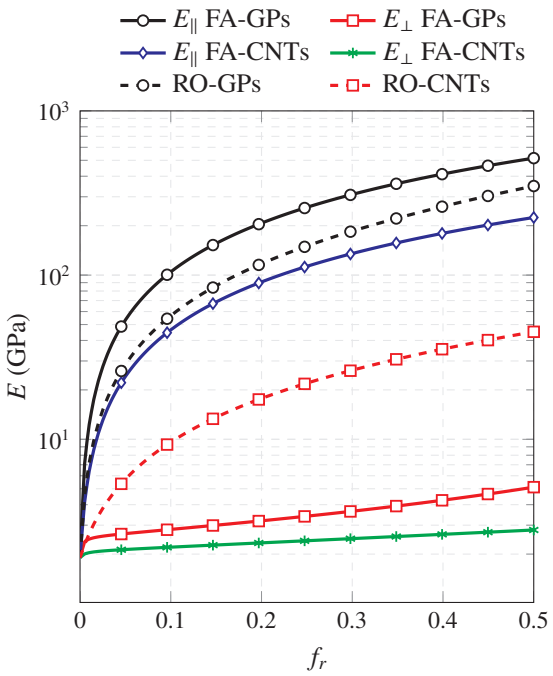

Figure 16: Elastic moduli versus filler content for UD GNP- and CNT-reinforced polymer composites with Fully Aligned (FA) and Randomly Oriented (RO) filler configurations.

6.2.3. Effect of agglomeration and restacking of graphene sheets on the bending and vibrational behavior of FG-GRC polymer plates

This set of analyses investigates the influence of defects in the microstructure of FG-GRCs, including agglomeration and restacking effects. Fig. 17 shows the non-dimensional central deflection $\bar{w}$ for UD GNP-reinforced polymer plates with different filler volume fractions, namely f_r = 0.05, 0.10, 0.15 and 0.20, as well as varying agglomeration degree and SSSS boundary conditions. The agglomeration parameter ξ is kept constant with value 0.2, while the remaining agglomeration parameter ζ ranges from 0 to 1. In other words, the ratio of spherical bundles with respect to the total volume of the RVE is fixed, while the filler distribution ranges between the limit cases of all the fillers dispersed outside and inside the bundles. The limit case of $\xi = \zeta = 0.2$ stands for perfectly uniform distribution, while the heterogeneity stems from the distinct filler concentrations within and outside the bundles. It is observed this figure that the agglomeration of fillers entails detrimental effects on the overall stiffness of the composite plates. Especially, large increases in the non-dimensional deflection are found for agglomeration parameters ζ above 0.8. The agglomeration of fillers in bundles can be thus understood as defects in the microstructure. The agglomeration effect on the non-dimensional fundamental frequency is also investigated in Fig. 18. In this case, the results for four linear functionally graded distributions, namely UD, FG-X, FG-V and FG-O are studied in Figs. 18 (a), (b), (c) and (d), respectively. It is evidenced that the agglomeration of GNPs induces detrimental effects on the macroscopic properties of the composites in all the cases. For instance, in the case of f_r = 0.2 and UD distribution, the limit case when all the nanofillers are gathered within the bundles yields reductions of the fundamental frequency up to 80% with respect to the uniform dispersion. This sort of results highlights the importance of developing efficient dispersion techniques to tackle the appearance of agglomerates which act as defects in the resulting microstructure. In this case, in a similar way to previous results, FG-X distribution leads to the highest frequency values.

The effect of non-linear distribution of the fillers across the thickness has been also studied for the particular case of FG-X distribution as shown in Fig. 19. As expected from previous analyses, it can be observed that higher power-law indexes, i.e. more fillers located at the top and bottom layers, lead to higher frequency values. However, it is also interesting to note that the agglomeration effects are more critical for higher power-law indexes where higher frequency reductions are registered.

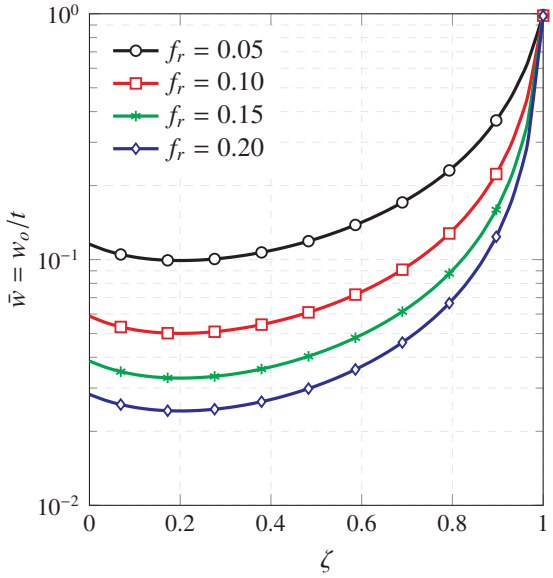

Figure 17: Non-dimensional central deflection of a composite plate reinforced by randomly oriented UD GNPs subjected to a uniform transverse loading $q_0 = 0.01$ MPa with agglomeration effects (UD, $\xi = 0.2$, $k = 1$, $a/b = 1$, $t = a/50$, SSSS).

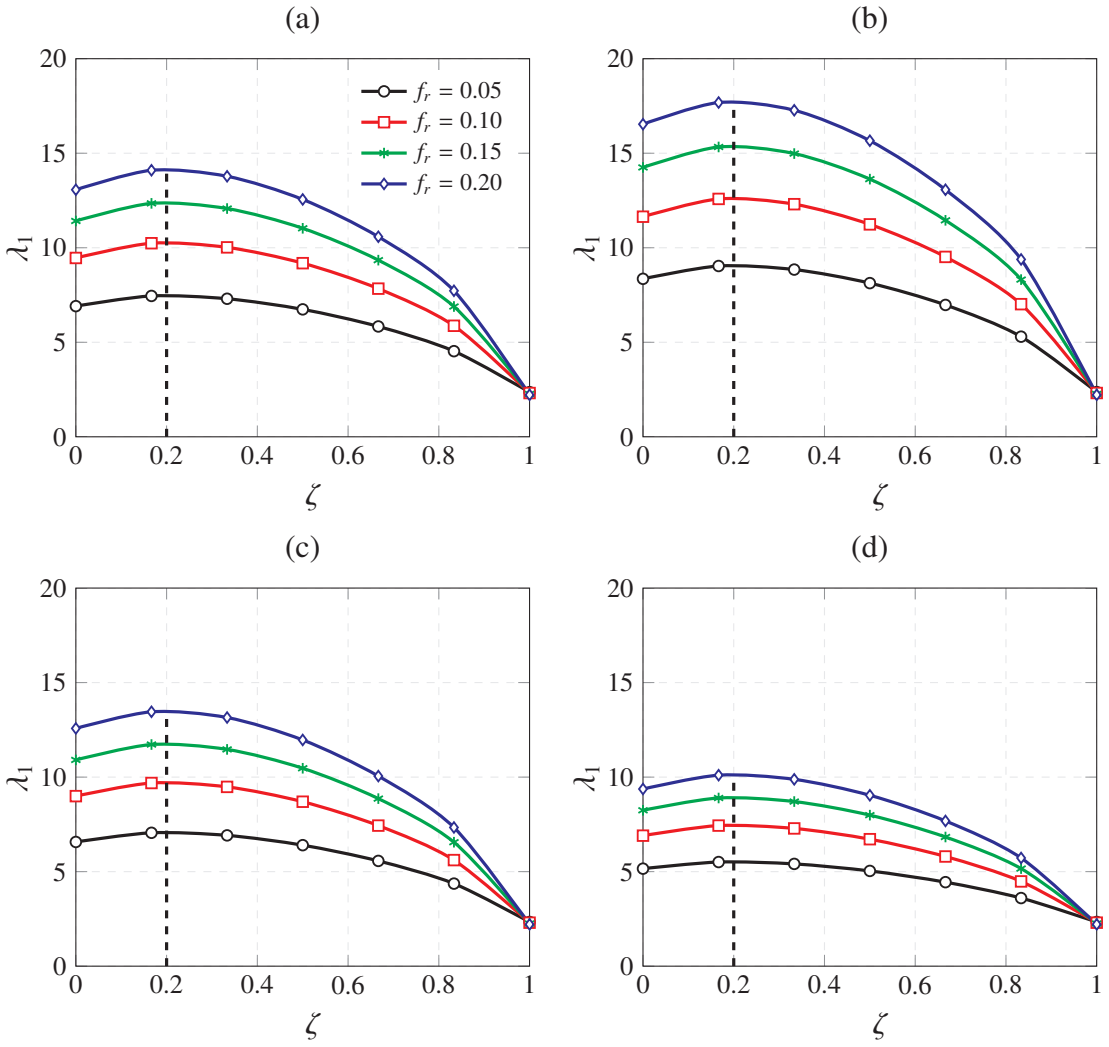

Figure 18: Non-dimensional fundamental frequency of a composite plate reinforced by randomly oriented UD (a), FG-X (b), FG-V (c) and FG-O (d) GNPs with agglomeration effects ($\xi = 0.2$, $k = 1$, $a/b = 1$, $t = a/50$, SSSS).

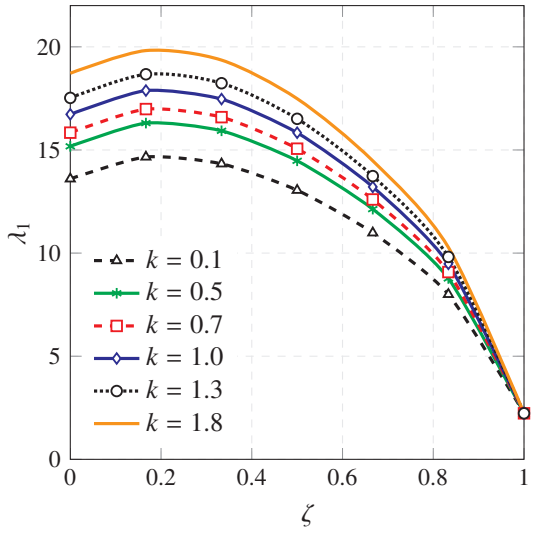

Figure 19: Non-dimensional fundamental frequency of a composite plate reinforced by randomly oriented FG-X GNPs with different power-law indexes k and agglomeration effects ($\xi = 0.2$, $a/b = 1$, $t = a/50$, SSSS).

The restacking effects on the non-dimensional central deflection and fundamental frequency of SSSS UD GRC plates are inspected in Figs. 20 and 21, respectively. Fully aligned and randomly oriented configurations are studied and denoted with solid and dashed lines, respectively. In accordance with Fig. 6, the restacking of graphene sheets forming multi-layered graphite platelets can be modeled by ellipsoidal inclusions with aspect ratios a_3/a_1. As previously discussed, graphene sheets can stack up forming multiple sheets. When tensile loads are transferred to the stacked graphene sheets, the vdW dispersion bonding between layers is likely to fail before graphitic carbon-carbon bonding, leading to further exfoliation of the particle. Hence, the material properties of the graphene sheets with restacking effects are taken as those defined for graphite in Table 1. It is extracted that for increasing number of stacked graphite layers, i.e. higher aspect ratio a_3/a_1, the overall stiffness decreases for both cases. It is especially critical for aspect ratios a_3/a_1 above E-3 where the most drastic reductions are found. These results evidence that the stiffening effect of graphene sheets may be dramatically reduced when a considerable fraction of fillers stacks up forming platelets of graphite.

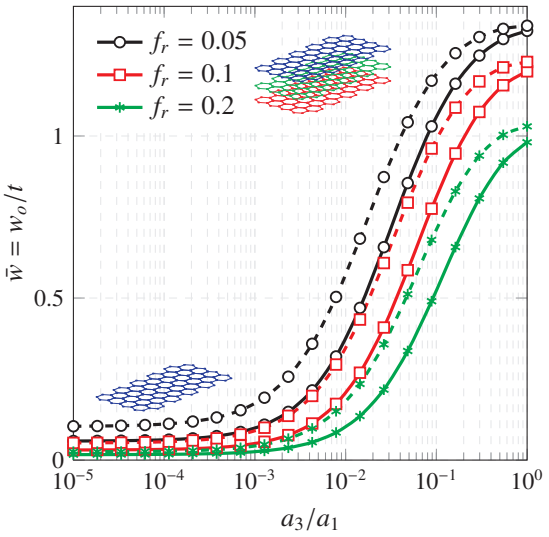

Figure 20: Non-dimensional central deflection of a composite plate reinforced by graphene sheets with restacking effects and subjected to an uniform transverse loading $q_0 = 0.01$ MPa (UD, $a/b = 1$, $t = a/50$, SSSS boundary condition, solid and dashed lines denote fully aligned and randomly oriented configurations, respectively).

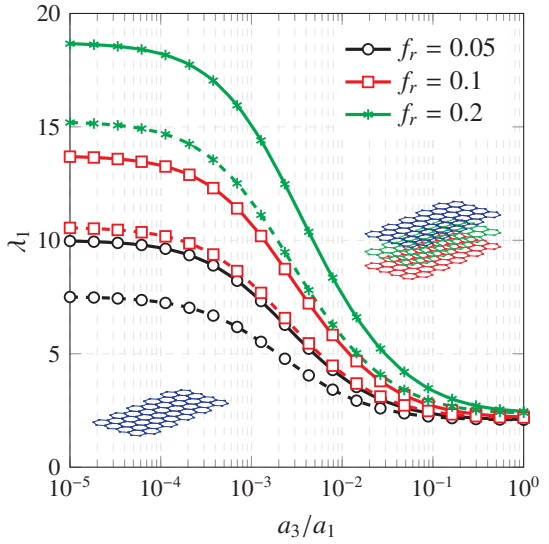

Figure 21: Non-dimensional fundamental frequency of a composite plate reinforced by graphene sheets with restacking effects (UD, $a/b = 1$, $t = a/50$, SSSS boundary condition, solid and dashed lines denote fully aligned and randomly oriented configurations, respectively).

7. Conclusions

This paper presents a study of the bending and vibrational behavior of FG-GRC plates by means of a Mori-Tanaka micromechanics model. A self-developed finite element code on the basis of FSDT plate elements have been used to conduct the numerical studies. Harmful effects reported in the literature such as agglomeration and restacking of graphene sheets have been considered. In order to highlight the superior load bearing capacity of GNPs compared to CNTs, detailed parametric analyses have been presented. Micromechanical aspects such as filler content, filler distribution, heterogeneous filler dispersions and restacking of graphene into graphite platelets have been investigated. Overall, the key findings of this work are summarized as follows:

- The stiffening effect of GNPs as mechanical additives have been shown superior in comparison to CNTs. In both fully aligned and randomly oriented configurations, graphene has been shown to provide stiffer macroscopic properties for the same filler content.
- The numerical results have demonstrated that functionally graded GNPs can tune the overall stiffness of the composite plates. In addition, it has been shown that fillers concentrated at the top and bottom layers of the plates lead to the highest natural frequencies.
- Agglomeration of fillers into clusters may be understood as a mechanical defect in the microstructure of the composite. The results demonstrated critical reductions of the resonant frequency as the heterogeneity degree of the filler dispersion increases.
- The restacking of graphene sheets into graphite platelets is a limiting factor of the macroscopic behavior of these composites. The numerical results showed dramatic reductions of the effective resonant frequencies for higher fractions of graphene sheets lumped into graphite platelets.

The present work is envisaged to provide a valuable theoretical framework to investigate the behavior of GRC structural elements. In virtue of a tractable analytical formulation, the present approach is readily applicable to an extensive range of structural elements, as well as to the design of high performance FG-GRCs.

Acknowledgement

This work was supported by the Ministerio de Economía y Competitividad of Spain, and the Consejería de Economía, Innovación, Ciencia y Empleo of Andalucía (Spain) under projects DPI2014-53947-R and P12-TEP-2546. E. G-M was also supported by a FPU contract-fellowship from the Spanish Ministry of Education Ref: FPU13/04892. The financial support is gratefully acknowledged.

References

[1] J. N. Coleman, U. Khan, W. J. Blau, Y. K. Gunko, Small but strong: a review of the mechanical properties of carbon nanotube–polymer composites, Carbon 44 (2006) 1624–1652.

[2] R. F. Gibson, A review of recent research on mechanics of multifunctional composite materials and structures, Composite Structures 92 (2010) 2793–2810.

[3] F. Ubertini, A. L. Materazzi, A. DAlessandro, S. Laflamme, Natural frequencies identification of a reinforced concrete beam using carbon nanotube cement-based sensors, Engineering Structures 60 (2014) 265–275.

[4] J. W. Lim, D. Lee, M. Kim, J. Choe, S. Nam, Composite structures for proton exchange membrane fuel cells (PEMFC) and energy storage systems (ESS), Composite Structures 134 (2015) 927–949.

[5] M. J. Lim, H. K. Lee, I. W. Nam, H. K. Kim, Carbon nanotube/cement composites for crack monitoring of concrete structures, Composite Structures 180 (2017) 741–750.

[6] I. W. Nam, S. M. Park, H. K. Lee, L. Zheng, Mechanical properties and piezoresistive sensing capabilities of FRP composites incorporating CNT fibers, Composite Structures 178 (2017) 1–8.

[7] M. Kaseem, K. Hamad, Y. G. Ko, Fabrication and materials properties of polystyrene/carbon nanotube (PS/CNT) composites: A review, European Polymer Journal 79 (2016) 36–62.

[8] Z. Spitalsky, D. Tasis, K. Papagelis, C. Galiotis, Carbon nanotube–polymer composites: Chemistry, processing, mechanical and electrical properties, Progress in Polymer Science 35 (2010) 357–401.

[9] D. Qian, E. C. Dickey, R. Andrews, T. Rantell, Load transfer and deformation mechanisms in carbon nanotube-polystyrene composites, Applied Physics Letters 76 (2000) 2868–2870.

[10] M. Martin-Gallego, M. M. Bernal, M. Hernandez, R. Verdejo, M. A. Lopez-Manchado, Comparison of filler percolation and mechanical properties in graphene and carbon nanotubes filled epoxy nanocomposites, European Polymer Journal 49 (2013) 1347–1353.

[11] G. Mittal, V. Dhand, K. Y. Rhee, S. J. Park, W. R. Lee, A review on carbon nanotubes and graphene as fillers in reinforced polymer nanocomposites, Journal of Industrial and Engineering Chemistry 21 (2015) 11–25.

[12] I. Zaman, H. C. Kuan, J. Dai, N. Kawashima, A. Michelmore, A. Sovi, S. Dong, L. Luong, J. Ma, From carbon nanotubes and silicate layers to graphene platelets for polymer nanocomposites, Nanoscale 4 (2012) 4578–4586.

[13] Z. Li, R. J. Young, N. R. Wilson, I. A. Kinloch, C. Valls, Z. Li, Effect of the orientation of graphene-based nanoplatelets upon the Young's modulus of nanocomposites, Composites Science and Technology 123 (2016) 125–133.

[14] M. A. Rafiee, J. Rafiee, Z. Wang, H. Song, Z. Z. Yu, N. Koratkar, Enhanced mechanical properties of nanocomposites at low graphene content, ACS nano 3 (2009) 3884–3890.

[15] S. Y. Yang, W. N. Lin, Y. L. Huang, H. W. Tien, J. Y. Wang, C. C. M. Ma, S. M. Li, Y. S. Wang, Synergetic effects of graphene platelets and carbon nanotubes on the mechanical and thermal properties of epoxy composites, Carbon 49 (2011) 793–803.

[16] S. Stankovich, D. A. Dikin, G. H. B. Dommett, K. M. Kohlhaas, E. J. Zimney, E. A. Stach, R. D. Piner, S. T. Nguyen, R. S. Ruoff, Graphene-based composite materials, Nature 442 (2006) 282–286.

[17] K. Kalaitzidou, H. Fukushima, L. T. Drzal, Mechanical properties and morphological characterization of exfoliated graphite-polypropylene nanocomposites, Composites Part A: Applied Science and Manufacturing 38 (2007) 1675–1682.

[18] T. Ramanathan, A. A. Abdala, S. Stankovich, D. A. Dikin, M. Herrera-Alonso, R. D. Piner, D. H. Adamson, H. C. Schniepp, X. R. R. S. Chen, R. S. Ruoff, Functionalized graphene sheets for polymer nanocomposites, Nature nanotechnology 3 (2008) 327–331.

[19] B. Das, K. E. Prasad, U. Ramamurty, C. N. R. Rao, Nano-indentation studies on polymer matrix composites reinforced by few-layer graphene, Nanotechnology 20 (2009) 125705.

[20] X. Y. Ji, Y. P. Cao, X. Q. Feng, Micromechanics prediction of the effective elastic moduli of graphene sheet-reinforced polymer nanocomposites, Modelling and Simulation in Materials Science and Engineering 18 (2010) 045005.

[21] K. N. Spanos, S. K. Georgantzinos, N. K. Anifantis, Mechanical properties of graphene nanocomposites: a multiscale finite element prediction, Composite Structures 132 (2015) 536–544.

[22] R. Rahman, A. Haque, Molecular modeling of crosslinked graphene-epoxy nanocomposites for characterization of elastic constants and interfacial properties, Composites Part B: Engineering 54 (2013) 353–364.

[23] C. Feng, S. Kitipornchai, J. Yang, Nonlinear free vibration of functionally graded polymer composite beams reinforced with graphene nanoplatelets (GPLs), Engineering Structures 140 (2017) 110–119.

[24] E. García-Macías, R. Castro-Triguero, E. I. S. Flores, M. I. Friswell, R. Gallego, Static and free vibration analysis of functionally graded carbon nanotube reinforced skew plates, Composite Structures 140 (2016) 473–490.

[25] P. Zhu, Z. Lei, K. M. Liew, Static and free vibration analyses of carbon nanotube-reinforced composite plates using finite element method with first order shear deformation plate theory, Composite Structures 94 (2012) 1450–1460.

[26] H. S. Shen, F. Lin, Y. Xiang, Nonlinear bending and thermal postbuckling of functionally graded graphene-reinforced composite laminated beams resting on elastic foundations, Engineering Structures 140 (2017) 89–97.

[27] Z. Zhao, C. Feng, Y. Wang, J. Yang, Bending and vibration analysis of functionally graded trapezoidal nanocomposite plates reinforced with graphene nanoplatelets (GPLs), Composite Structures 180 (2017) 799–808.

[28] B. Yang, S. Kitipornchai, Y. F. Yang, J. Yang, 3D thermo-mechanical bending solution of functionally graded graphene reinforced circular and annular plates, Applied Mathematical Modelling 49 (2017) 69–86.

[29] M. Song, J. Yang, S. Kitipornchai, W. Zhu, Buckling and postbuckling of biaxially compressed functionally graded multilayer graphene nanoplatelet-reinforced polymer composite plates, International Journal of Mechanical Sciences 131 (2017) 345–355.

[30] W. Li, A. Dichiara, J. Bai, Carbon nanotube-graphene nanoplatelet hybrids as high-performance multifunctional reinforcements in epoxy composites, Composites Science and Technology 74 (2013) 221–227.

[31] J. A. King, D. R. Klimek, I. Miskioglu, G. M. Odegard, Mechanical properties of graphene nanoplatelet/epoxy composites, Journal of Applied Polymer Science 128 (2013) 4217–4223.

[32] A. Allaoui, S. Bai, H. Cheng, J. Bai, Mechanical and electrical properties of a MWNT/epoxy composite, Composites Science and Technology 62 (2002) 1993–1998.

[33] H. Li, H. Xiao, J. Yuan, J. Ou, Microstructure of cement mortar with nano-particles, Composites Part B: Engineering 35 (2004) 185–189.

[34] J. M. Wernik, S. A. Meguid, Recent developments in multifunctional nanocomposites using carbon nanotubes, Applied Mechanics Reviews 63 (2010) 050801.

[35] D. Shi, X. Feng, Y. Y. Huang, K. Hwang, H. Gao, The effect of nanotube waviness and agglomeration on the elastic property of carbon nanotube-reinforced composites, Journal of Engineering Materials and Technology 126 (2004) 250–257.

[36] F. Tornabene, N. Fantuzzi, M. Bacciocchi, E. Viola, Effect of agglomeration on the natural frequencies of functionally graded carbon nanotube-reinforced laminated composite doubly-curved shells, Composites Part B: Engineering 89 (2016) 187–218.

[37] F. Tornabene, M. Bacciocchi, N. Fantuzzi, J. Reddy, Multiscale approach for three-phase CNT/polymer/fiber laminated nanocomposite structures, Polymer Composites (2017).

[38] E. García-Macías, A. D'Alessandro, R. Castro-Triguero, D. Pérez-Mira, F. Ubertini, Micromechanics modeling of the uniaxial strain-sensing property of carbon nanotube cement-matrix composites for SHM applications, Composite Structures 163 (2017) 195–215.

[39] B. Sobhaniaragh, M. Nejati, W. J. Mansur, Buckling modelling of ring and stringer stiffened cylindrical shells aggregated by graded CNTs, Composites Part B: Engineering 124 (2017) 120–133.

[40] E. García-Macías, L. Rodríguez-Tembleque, R. Castro-Triguero, A. Sáez, Eshelby-Mori-Tanaka approach for post-buckling analysis of axially compressed functionally graded CNT/polymer composite cylindrical panels, Composites Part B: Engineering 128 (2017) 208–224.

[41] A. Fasolino, J. H. Los, M. I. Katsnelson, Intrinsic ripples in graphene, Nature materials 6 (2007) 858–861.

[42] J. C. Meyer, A. K. Geim, M. I. Katsnelson, K. S. Novoselov, T. J. Booth, S. Roth, The structure of suspended graphene sheets, Nature 446 (2007) 60–63.

[43] E. Perim, L. D. Machado, D. S. Galvao, A brief review on syntheses, structures and applications of nanoscrolls, Frontiers in Materials 1 (2014) 31.

[44] S. Nemat-Nasser, M. Hori, Micromechanics: overall properties of heterogeneous materials, volume 37, Elsevier, 2013.

[45] R. Hill, A self-consistent mechanics of composite materials, Journal of the Mechanics and Physics of Solids 13 (1965) 213–222.

[46] T. Mori, K. Tanaka, Average stress in matrix and average elastic energy of materials with misfitting inclusions, Acta metallurgica 21 (1973) 571–574.

[47] J. D. Eshelby, The determination of the elastic field of an ellipsoidal inclusion, and related problems, Proceedings of the Royal Society of London. Series A. Mathematical and Physical Sciences 241 (1957) 376–396.

[48] J. Eshelby, The elastic field outside an ellipsoidal inclusion, Proceedings of the Royal Society of London. Series A, Mathematical and Physical Sciences (1959) 561–569.

[49] Y. Benveniste, A new approach to the application of Mori-Tanaka's theory in composite materials, Mechanics of Materials 6 (1987) 147–157.

[50] T. Mura, Micromechanics of defects in solids, volume 3, Springer Science & Business Media, 1987.

[51] J. Cho, J. J. Luo, I. M. Daniel, Mechanical characterization of graphite/epoxy nanocomposites by multi-scale analysis, Composites science and technology 67 (2007) 2399–2407.

[52] E. Efraim, M. Eisenberger, Exact vibration analysis of variable thickness thick annular isotropic and FGM plates, Journal of Sound and Vibration 299 (2007) 720–738.

[53] C. Lee, X. Wei, J. W. Kysar, J. Hone, Measurement of the elastic properties and intrinsic strength of monolayer graphene, science 321 (2008) 385–388.

[54] C. D. Reddy, S. Rajendran, K. M. Liew, Equilibrium configuration and continuum elastic properties of finite sized graphene, Nanotechnology 17 (2006) 864.

[55] V. Popov, V. Van Doren, M. Balkanski, Elastic properties of crystals of single-walled carbon nanotubes, Solid State Communications 114 (2000) 395–399.

[56] O. L. Blakslee, D. G. Proctor, E. J. Seldin, G. B. Spence, T. Weng, Elastic constants of compression-annealed pyrolytic graphite, Journal of Applied Physics 41 (1970) 3373–3382.

[57] E. T. Thostenson, T. W. Chou, On the elastic properties of carbon nanotube-based composites: modelling and characterization, Journal of Physics D: Applied Physics 36 (2003) 573.

[58] E. Hinton, Numerical methods and software for dynamic analysis of plates and shells, Pineridge Press, 1988.

[59] K. M. Liew, J. Wang, T. Y. Ng, M. J. Tan, Free vibration and buckling analyses of shear-deformable plates based on FSDT meshfree method, Journal of Sound and Vibration 276 (2004) 997–1017.

[60] A. Choudhury, Preparation and characterization of nanocomposites of poly-p-phenylene benzobisthiazole with graphene nanosheets, RSC Advances 4 (2014) 8856–8866.

[61] J. Affdl, J. Kardos, The Halpin-Tsai equations: a review, Polymer Engineering & Science 16 (1976) 344–352.

[62] M. A. Van Es, Polymer-clay nanocomposites: the importance of particle dimensions, Ph.D. thesis, Delft, The Netherlands: Delft University of Technology, 2001.

[63] D. Villoria, R. Guzman, A. Miravete, Mechanical model to evaluate the effect of the dispersion in nanocomposites, Acta Materialia 55 (2007) 3025–3031.

[64] W. Voigt, Ueber die beziehung zwischen den beiden elasticittsconstanten isotroper krper, Annalen der Physik 274 (1889) 573–587.

[65] A. Reuss, Calculation of the flow limits of mixed crystals on the basis of the plasticity of monocrystals, Z. Angew. Math. Mech 9 (1929) 49–58.

[66] Z. Hashin, S. Shtrikman, A variational approach to the theory of the elastic behaviour of multiphase materials, Journal of the Mechanics and Physics of Solids 11 (1963) 127–140.

[67] L. Walpole, On the overall elastic moduli of composite materials, Journal of the Mechanics and Physics of Solids 17 (1969) 235–251.

[68] S. Wu, R. B. Ladani, J. Zhang, E. Bafekrpour, K. Ghorbani, A. P. Mouritz, A. J. Kinloch, C. H. Wang, Aligning multilayer graphene flakes with an external electric field to improve multifunctional properties of epoxy nanocomposites, Carbon 94 (2015) 607–618.

[69] M. S. Al-Haik, H. Garmestani, D. S. Li, M. Y. Hussaini, S. S. Sablin, R. Tannenbaum, K. Dahmen, Mechanical properties of magnetically oriented epoxy, Journal of Polymer Science Part B: Polymer Physics 42 (2004) 1586–1600.

[70] Y. Qiu, G. Weng, On the application of Mori-Tanaka's theory involving transversely isotropic spheroidal inclusions, International Journal of Engineering Science 28 (1990) 1121–1137.

[71] M. Song, S. Kitipornchai, J. Yang, Free and forced vibrations of functionally graded polymer composite plates reinforced with graphene nanoplatelets, Composite Structures 159 (2017) 579–588.